CME LIVE OPEN ACCESS

International Journal of Material Science

Research Article

Preparation of Fe_2O_3-Polypyrrole and NiO- Polypyrrole Nanocomposite Materials for the Photocatalytic Generation of Hydrogen

Thembalethu N. Mkhonza*, L. Legapa Nkabiti, Rebotsamang F. Shago and Mpho W. Mathebula

Department of Chemistry, University of the Free State, Bloemfontein, South Africa.

Corresponding Author: T N Mkhonza, Department of Chemistry, University of the Free State, Bloemfontein, South Africa.

Received: 2026 Apr 24 **Accepted:** 2026 May 24 **Published:** 2026 July 10

Abstract

Exploration of clean energy and carbon-free fuels is motivated by the pressing need for decarbonization, with hydrogen largely emerging as a solution. Photocatalysis provides a simple and environmentally friendly method for energy conversion and environmental cleanup by generating hydrogen from ammonia. Plant-mediated synthesized nanomaterials are becoming increasingly more popular because of their superior physicochemical properties, availability, ease of application, ease of preparation, and environmental friendliness. This article investigates the conductivity and efficiency of Fe_2O_3 and NiO nanoparticles coupled with pyrrole to form nanocomposites which were synthesized using Spinacia oleracea and Moringa oleifera as plant extracts acting as stabilizers and reducing agents in nanoparticle synthesis. Using biomaterials, the nanocomposites were successfully synthesized, and their structure, morphology, and composition were analyzed using characterization methods such as XRD, FTIR, UV-Vis, CV, and SEM. This thorough characterization highlighted the potential of these nanocomposites for use in hydrogen generation in the future.

Keywords: Photocatalysis, Hydrogen, Ammonia Degradation, Metal Oxide Nanoparticles, Decarbonization, Green Synthesis

1. Introduction

Today, the generation of electricity worldwide heavily relies on fossil fuels, which are non-renewable resources that take longer to recharge or reoccur to their previous capacity [1-11]. It is widely recognized that our existing energy infrastructure, which is heavily dependent on fossil fuels, is not sustainable. It is incapable of accommodating the projected increase in population and the corresponding rise in energy consumption per individual without causing environmental harm and intensifying the effects of global warming [5]. From 1970 to 2010, approximately 78 % of the increase in greenhouse gas emissions was due to CO emissions from fossil fuel combustion and industrial activities. During this period, atmospheric CO concentrations rose from about 325 ppm to roughly 400 ppm, while the average global temperature climbed by approximately 0.56°C. To stabilize these trends and keep atmospheric CO levels below 440 ppm by 2050, it is crucial to significantly cut CO emissions from fossil fuel combustion. One of the primary strategies to reduce harmful emissions is the adoption of a hydrogen economy [12-25]. This approach offers a comprehensive view of low-cost clean energy and extensive decarbonization across various sectors.

Hydrogen, the most basic and abundant element in the universe, can be utilized in fuel cells to produce electricity and power vehicles without emitting carbon oxides (COx) and nitrogen oxides (NOx), in addition to providing backup power and grid stabilization [26-29]. However, storing hydrogen poses a significant challenge despite extensive global efforts, due to its low volumetric energy density of 3 Wh/L [25]. A major issue is that hydrogen does not naturally occur in its pure form on earth, necessitating its production from hydrogen-containing compounds like water or hydrocarbons, a process that can demand considerable energy [20]. Additionally, hydrogen can be chemically stored in various molecules, including methanol, methane, metal amine salts (e.g., Mg $(NH_3)_6$ Cl_2), ammonia, and related compounds (e.g., NH_3BH_3), or in hydrides (such as $LaNi_5H_6$ or complex hydrides like $NaAlH_4$) [6].

Ammonia (NH_3) stands out as one of the carbon-free compounds that, upon dehydration, yields only nitrogen and hydrogen as byproducts. It has a high volumetric hydrogen storage density (108 kg H_2 m^{-3} NH_3 liquid), a gravimetric hydrogen storage density of 17.8 wt%, and it can be liquefied at 20 °C under 8.6 bar. Furthermore, the ammonia process is well-established, making ammonia a promising candidate for hydrogen energy storage.

Ammonia decomposition provides a workable on-site alternative to hydrogen production, hence addressing the main disadvantage of hydrogen storage and transportation that are preventing its universal implementation [18]. The

decomposition of ammonia to produce hydrogen requires substantial heat absorption, with ammonia beginning to decompose into hydrogen and nitrogen above 200 °C, and complete conversion occurring above 650 °C, a temperature unsuitable for current hydrogen fuel cells [30-42]. Therefore, the development of effective catalysts to enhance the kinetics of hydrogen production from ammonia decomposition at lower temperatures is vital for advancing hydrogen fuel cell applications. The catalytic decomposition of ammonia is essentially the reverse of the Haber-Bosch process, a well-researched method over the last 150 years. The metal platinum, palladium, rhodium, and ruthenium were initially explored as catalysts for ammonia decomposition. More metals were explored in the catalytic performance with respect to ammonia decomposition, and their activity was determined in the following order from highest to lowest: Ru > Rh > Co >Ir >Fe > Pt >Cr > Pd > Cu >> Te, Se, Pb [30]. This article aims to explore the approach of using biosynthetically prepared polymer-metallic oxide as promising catalysts for ammonia decomposition.

The green synthesis method is one of the most promising and ecologically friendly ways to synthesize nanoparticles. Green synthesis methods frequently use relatively safe resources, like water, biological extracts, and microwave-assisted synthesis, to produce nanomaterials. It makes use of biological agents like bacteria, fungi, and plant extracts. However, a variety of nanoparticles have been synthesized using plant components, such as fruits, stems, leaves, seeds, and roots. Additionally, some green materials can be utilized as both dispersants and end-capping agents, which not only saves energy but also minimizes the need for hazardous and toxic chemicals. Green materials contain proteins and polyphenols that can be used as reducing agents in place of chemical reagents to lower the valence state of metal ions [43]. The ultimate shape and size of the nanoparticle are determined by several active molecules and precursors, including metal salts. Biosynthesis of nanoparticles using bio-green technologies provides several advantages over chemical and physical synthesis methods in terms of effectiveness, cleanliness, simplicity, non-toxicity, low cost, and environmental friendliness [39]. Furthermore, the advantages of green synthesis for nanoparticles include antibacterial, reducing, and stabilizing qualities [22]. Given these advantages, this research will focus on leaf (*Moringa oleifera* and *Spinacia oleracea*) extraction for the synthesis of nanoparticles photocatalysts.

Catalytic ammonia decomposition is a common hydrogen production technology. Various technologies, such as thermocatalytic NH_3 decomposition, photocatalytic NH_3 decomposition, plasma-catalytic NH_3 decomposition, and electrocatalytic NH_3 decomposition, have been designed to generate clean H_2 [21]. These catalysts include a second catalytic metal, a promoter, a support, and/or a transition metal. When evaluating various catalysts, a number of factors must be taken into account, including cost, long-term stability, efficiency, oxides or alloys, and catalysts made of pure metals. This includes precious or noble metals as well as non-precious metals depending on their price, type and characteristics. This article focuses on photocatalytic NH_3 decomposition as a promising method that utilizes sunlight to drive the reaction under normal conditions. In this article our main focus is the electrochemical and physicochemical characterization of F_2O_3, NiO and their pyrrole-based composites synthesized via green synthesis method for possible use in the decomposition of ammonia.

2. Materials and Reagents

Ferric chloride hexahydrate ($FeCl_3{\cdot}6H_2O$), nickel(II) chloride ($NiCl_2$), sodium hydroxide (NaOH), potassium persulfate ($K_2S_2O_8$, ammonia (NH_3, 32%), ethanol (C_2H_6O, 95%), pyrrole (C_4H_5N). For this experiment, every chemical reagent utilized was of analytical grade.

2.1. Synthesis Procedure

2.1.1. Preparation of *Moringa Oliefera* Extract

Fresh leaves of *Moringa oleifera* were collected and washed with deionised water to get rid of any debris that might be attached. To avoid thermal degradation of the bioactive compounds, the leaves were dried in a shaded area before being weighed (Figure 1A). The dried leaves were then chopped into fine pieces and ground into fine powder (Figure 1B). 20.396 g of leaf powder was weighed and stirred in a mixture of 100 mL of distilled water and 100 mL of ethanol. The mixture was then incubated at room temperature for 24 hours (Figure 1C). After incubation, using a Whatmann no.1 filter paper, the solution was thoroughly filtered (Figure 1D) [16].

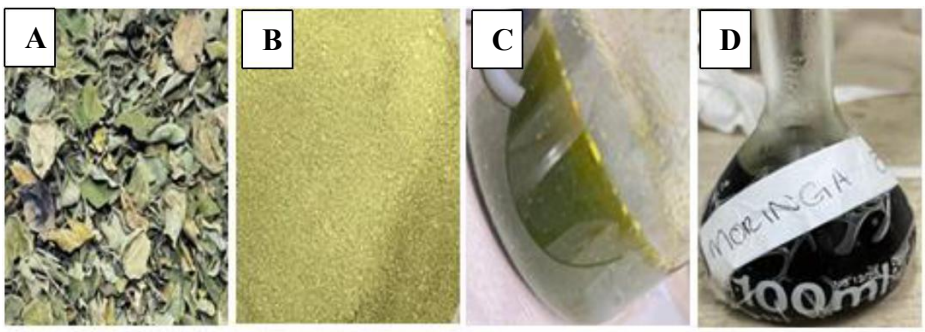

Figure 1: Depiction of (A) The Dried Leaves of *Moringa oleifera* , (B) The Ground Leaves of *Moringa Oleifera* , (C) The Solution Mixture After Incubation, (D) The *Moringa Oleifera* Extract After Filtering

2.1.2. Preparation of *Spinacia Oleracea* Extract

The leaves were carefully separated from the stem and washed with deionized water (Figure 2A). The leaves were dried in an oven at 80 $_{o}$C and ground into powder (Figure 2B). 25.134 g of Spinacia oleracea powder was boiled in 250 mL of distilled water in an Erlenmeyer flask under constant stirring for 15 minutes. The extract was cooled to room temperature, and it was filtered with Whatman no.1 filter paper (Figure 2C & D) [31].

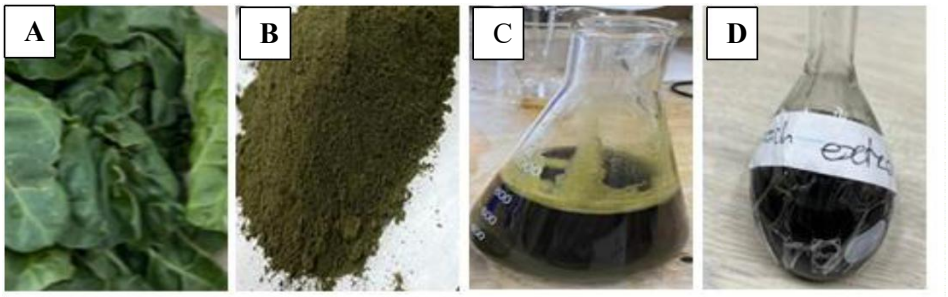

Figure 2: Depiction of (A) The Washed *Spinacia Oleracea* Leaves, (B) The *Spinacia Oleracea* Leaves After Being Ground, (C) The *Spinacia Oleracea* Leaf Extract After Being Cooled Before Filtering, and (D) The *Spinacia Oleracea* Extract After Being Filtered

2.1.3. Preparation of Plant-Mediated Metal Oxide Nanoparticles

0.01 mol of metal precursor ($FeCl_3{\cdot}6H_2O$ or $NiCl_2$) was weighed and dissolved in 100 mL of distilled water in a 250-mL beaker and heated at 80 $_{o}$C on a hot plate with continuous stirring. A 20-mL aqueous solution of the plant extract was added to the mixture after 10 minutes, which led to a visible colour change. To enable uniform precipitation of the metal oxide, 20 mL of an aqueous solution of sodium hydroxide (1.25 M) was added to the mixture at a rate of 3 mL per minute, whereafter the reaction mixture was left to cool to room temperature. The mixture was centrifuged at 5000 rpm for 45 minutes and then rinsed three times with deionised water to obtain metal oxide nanoparticles, then the metal oxide precipitate was left to dry overnight at 60 $_{o}$C. The dried-up sample was calcined for 5 hours at 500 $_{o}$C to eliminate organic impurities, increase crystallinity, and strengthen structural stability [31].

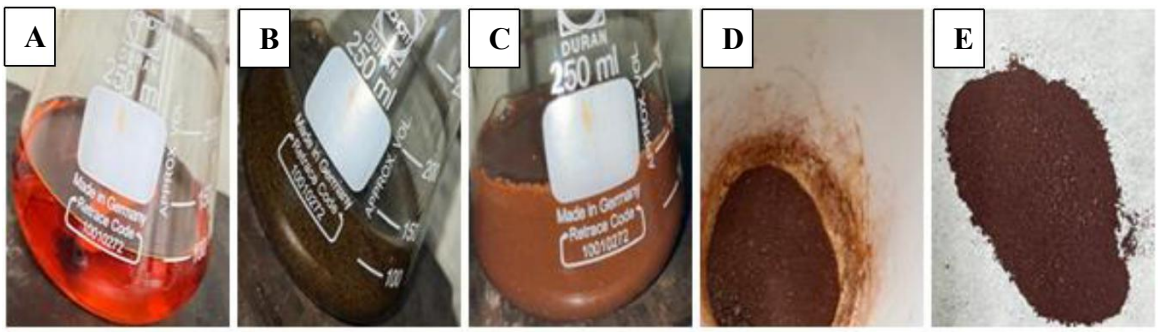

Figure 3: Depiction of the synthesis steps of Fe_2O_3 nanoparticles using *Spinacia oleracea* plant extract. (A) Solution after $FeCl_3{\cdot}6H_2O$ was added to distilled water, (B) the reaction mixture after *Spinacia oleracea* was added, (C) the reaction mixture after the addition of NaOH, (D) the dried Fe_2O_3 nanoparticles before calcination, and (E) the final product of Fe_2O_3 nanoparticles after calcination

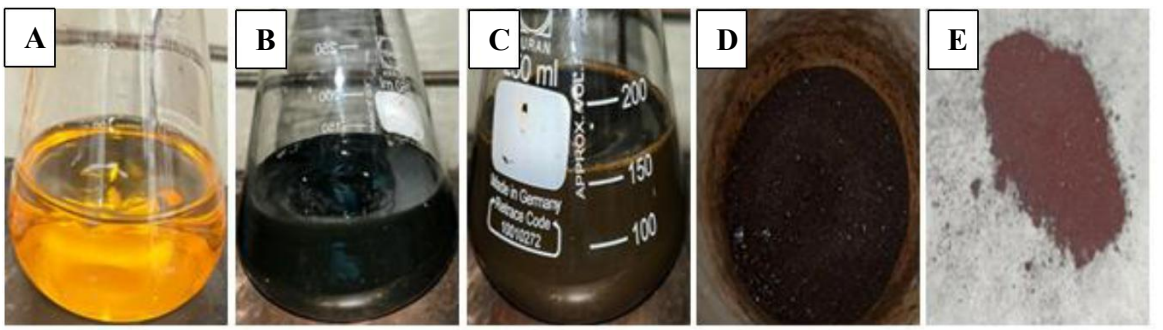

Figure 4: Depiction of the synthesis steps of Fe_2O_3 nanoparticles using *Moringa oleifera* plant extract. (A) Solution after $FeCl_3{\cdot}6H_2O$ was added to distilled water, (B) the reaction mixture after *Moringa oleifera* was added, (C) the reaction mixture after the addition of NaOH, (D) the dried Fe_2O_3 nanoparticles before calcination, and (E) the final product of Fe_2O_3 nanoparticles after calcination

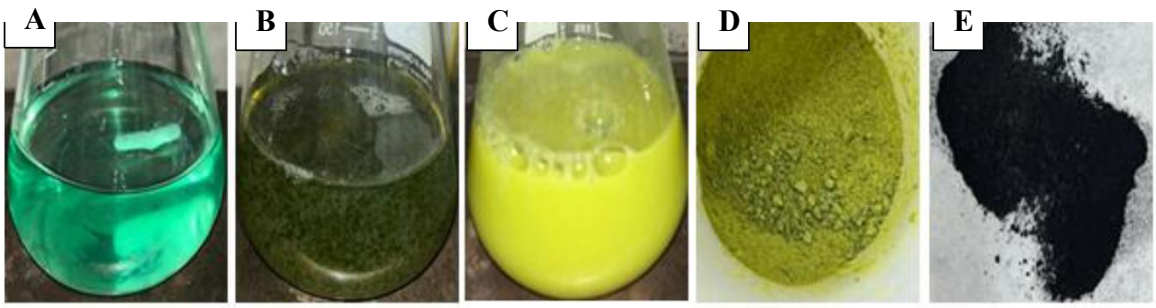

Figure 5: Depiction of the synthesis of NiO nanoparticles using *Spinacia oleracea* plant extract. (A) Solution after $NiCl_2$ was added to distilled water, (B) the reaction mixture after *Spinacia oleracea* was added, (C) the reaction mixture after the addition of NaOH, (D) the dried NiO nanoparticles before calcination, and (E) the final product of NiO nanoparticles after calcination

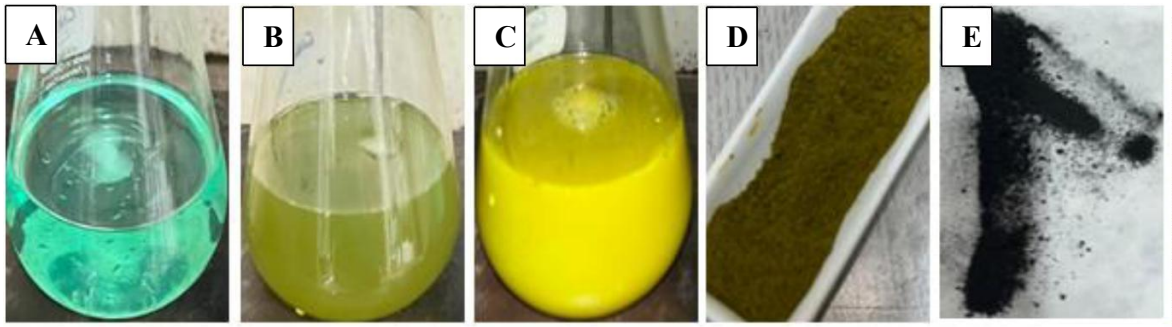

Figure 6: Depiction of the synthesis of NiO nanoparticles using *Moringa oleifera* plant extract. (A) Solution after $NiCl_2$ was added to distilled water, (B) the reaction mixture after *Moringa oleifera* was added, (C) the solution mixture after the addition of NaOH, (D) the dried NiO nanoparticles before calcination, and (E) the final product of NiO nanoparticles after calcination

2.1.4. Preparation of Polypyrrole

Polypyrrole was synthesized by chemical oxidative precipitation in aqueous medium. 150 g of water and 1.5 g of pyrrole were added into a 200 mL reaction flask. The monomer solution was then mixed with an aqueous solution of KPS (14.1 g in 30 g water), giving a monomer/KPS molar ratio of 3/7. With continuous stirring, the polymerization process ran for 24 hours at 25 °C, yielding black products. The residual monomer and any oligomers were eliminated by centrifuging the reaction mixture at 5000 rpm for 45 minutes and then washing three times with deionised water. Following the supernatant's removal, the black sediment was dried overnight in an oven at 60 °C [35].

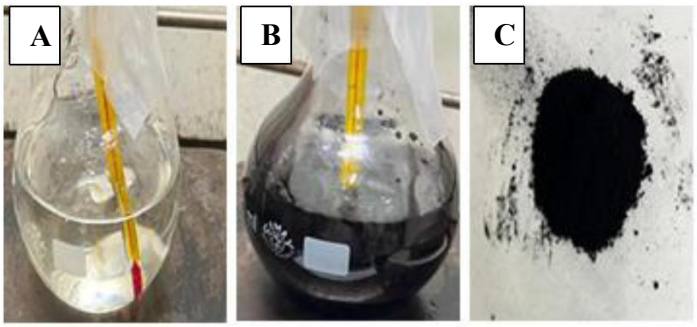

Figure 7: Depiction of the synthesis of polypyrrole. (A) The reaction mixture after the addition of pyrrole and KPS solution, (B) the reaction mixture after the polymerization process was completed, and (C) the final polypyrrole product

2.1.5. Preparation of Polypyrrole Composites

Fe_2O_3 and NiO nanoparticles that had been previously produced were used to synthesize polypyrrole composites. 50 mg of the nanoparticle sample and pyrrole (21 mg (Fe_2O_3) / 41.9 mg (NiO)) were mixed with 100 ml of distilled water in a 1:1 molar ratio. After that, the reaction mixture was sonicated for half an hour. Following sonication, an aqueous solution of KPS (0.198 g (Fe_2O_3) / 0.422g (NiO) in 20 mL of deionised water; monomer/KPS molar ratio: 3/7) was added to the reaction mixture. With continuous stirring, the

polymerization process ran for 24 hours at 25 °C, yielding black products. The residual monomer and any oligomers were eliminated by centrifuging the reaction mixture at 5000 rpm for 45 minutes and then washing three times with deionised water. Following the supernatant's removal, the black sediment was dried overnight in an oven at 60 °C.

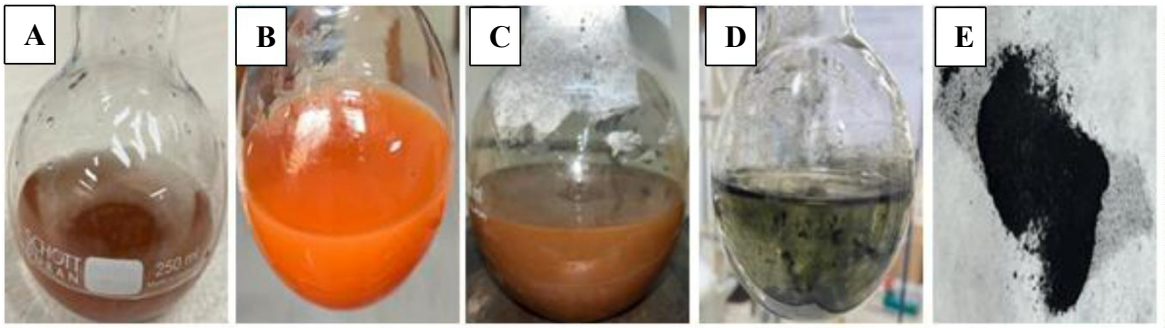

Figure 8: Depiction of the synthesis of Fe_2O_3-polypyrrole nanocomposite. (A) The reaction mixture after Fe_2O_3 nanoparticles and pyrrole have been added to water, (B) the reaction mixture after sonication, (C) the reaction mixture after the addition of KPS solution, (D) the reaction mixture after polymerization, and (E) the final product

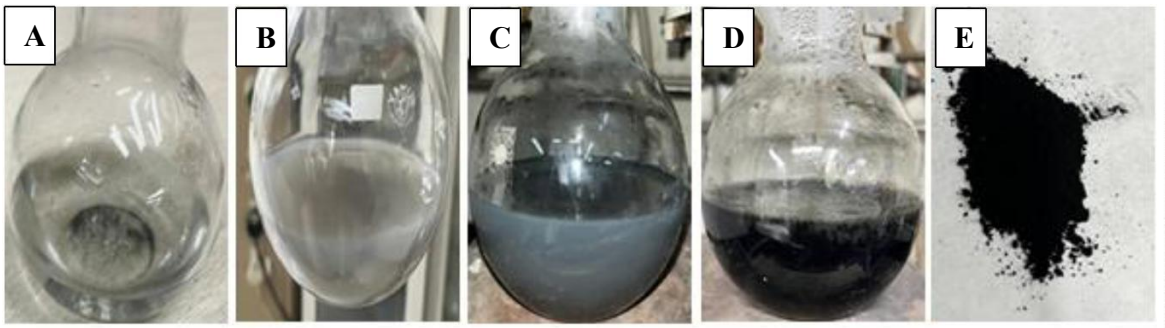

Figure 9: Depiction of the synthesis of NiO-polypyrrole nanocomposite. (A) The reaction mixture after NiO nanoparticles and pyrrole have been added to water, (B) the reaction mixture after sonication, (C) the reaction mixture after the addition of KPS solution, (D) the reaction mixture after polymerization, and (E) the final product

3. Characterization Techniques

3.1. Fourier-Transform Infrared (FTIR)

Fourier-Transform Infrared spectroscopy (FTIR) is an instrumental method that measures the absorption of infrared light across a range of wavelengths to determine the functional groups found in both organic and inorganic molecules [7].

A thermos Scientific Nicolet iS50 Ft-IR spectrometer was used to record the spectra, which were in the range 4000-400 cm^{-1}. The Attenuated Total Reflectance (ATR) method was used for analysis. The characteristic absorption bands that corresponded to the functional groups in the sample were identified using the obtained spectra.

3.2. X-Ray Diffraction (XRD)

X-ray diffraction (XRD) is a potent non-destructive method for crystalline material characterization. It offers details on phases, structures, preferred orientations (texture), and other structural factors like average grain size, crystallinity, strain, and crystal defects. X-ray diffraction peaks are caused by constructive interference of a monochromatic X-ray beam dispersed at particular angles from each pair of lattice planes in a sample. The arrangement of atoms within the lattice determines the peak intensities. The fingerprint of periodic atomic configurations in a particular material is hence the X-ray diffraction pattern [10].

A PANalytical Aeris X-ray diffractometer with a Cu Kα radiation source working at 40 kV and 7.5 mA was used for the characterization. The diffraction patterns were recorded over a 2θ range of 10°-80° . Powdered samples were placed on a flat sample holder. The resulting diffraction patterns were used to determine the materials' crystalline phases that were present.

3.3. Ultraviolet-Visible (UV-Vis)

UV-Vis spectroscopy is an analytical method which measures the number of distinct UV or visible light wavelengths that a sample absorbs or transmits when compared to a reference or blank sample. The composition of the sample affects this property, which may reveal information about the contents and concentrations of the sample.

A Varian Cary 50 Conc. UV-Visible Spectrophotometer was used for the measurements. The absorption spectra were obtained over a range of 200-800 nm. The sample was prepared by dissolving the substance in 98% ethanol and then putting them in a quartz cuvette that was 1 cm long. The material's optical characteristics and electronic transitions

were shown by analysing the recorded spectra to find distinctive absorption bands.

3.4. Scanning Electron Microscope (SEM)

SEM is a significant electron microscopy method that can produce a high-quality, spatially resolved visual image of a particle. It is a multifunctional, cutting-edge tool that is frequently used to examine material surface phenomena. SEM is a helpful tool for material characterization because it exposes the sample to a high-energy electron beam, which provides information about the material's topography, morphology, composition, chemistry, grain orientation, crystallographic information, etc [3].

For imaging, a JOEL JSM-6610 SEM was used. The powder sample was mounted on an aluminium stub using carbon tape. The stub was then placed in a sputter coater, where the sample was coated with iridium. After coating, the sample was ready for SEM analysis. The obtained image gave detailed information about the materials' microstructure.

3.5. Particle Size Analysis

ImageJ program was used to calculate the sample's average particle size. Images from Scanning Electron Microscopy (SEM) with a 100 µm scale bar were imported into the software and calibrated using the given scale (100 µm) in order to achieve accurate measurements. Individual particles visible in each image were manually measured using the particle analysis tools in ImageJ. This procedure was repeated for the other SEM images of the other samples. The average particle size of each sample was then determined from the measured particle sizes obtained from each image.

3.6. Cyclic Voltammetry (CV)

Cyclic voltammetry is an effective and widely used electrochemical method for studying the reduction and oxidation processes of molecules. Additionally, CV is very useful for studying chemical reactions that are triggered by electron transport, such as catalysis. In a cyclic voltammetry experiment, the current is measured while a working electrode's potential is linearly scanned in both forward and backward directions with respect to a reference electrode [15].

A Bas 100 Electrochemical Analyzer was used to conduct cyclic voltammetry measurements in order to assess the sample's conductivity and electrochemical activity. A typical three-electrode electrochemical cell was used, including a working electrode, a platinum counter electrode, and an Ag/AgCl reference electrode immersed in 3M sodium chloride solution. The potential was scanned from -500 mV to +1000 mV and the back to -500 mV to complete the cycle. The current response was measured using a scan rate of 50 mVs^{-1} and a sensitivity of 100 μAV^{-1}. The material's conductivity was examined using the current-potential curves that were produced by cyclic voltammetry.

4. Results and Discussion

4.1. FTIR Spectroscopic Analysis

FTIR was recorded at room temperature in order to analyze the dominant functional groups found in the synthesized nanoparticles, their polypyrrole-based composites, and polypyrrole.

4.2. Fe_2O_3 Nanoparticles and their Composites

Figure 10 depicts the FTIR spectra of the synthesized Fe_2O_3-based nanoparticles, their polypyrrole-based composites, and pure polypyrrole, obtained in the 400-4000 cm^{-1} wavenumber region. The spectra provide information about the functional groups and chemical bonds present in the materials. All four Fe_2O_3-based materials exhibit a consistent absorption band at approximately 3000 cm^{-1}, which is attributed to O-H stretching vibrations. In comparison to the pure Fe_2O_3-based materials (Fe_2O_3-Mor and Fe_2O_3-Spin), this band is significantly more intense in the composite materials (Fe_2O_3-Pyrr-Mor and Fe_2O_3-Pyrr-Spin). The increased intensity is because there is an overlap of two functional groups, the O-H stretching vibration which is due to surface adsorbed water and the N-H stretching vibration which confirms the incorporation of polypyrrole. This band is also present in the pure polypyrrole spectrum, further supporting this interpretation. The asymmetric and symmetric bending vibration of C=O groups are represented as absorption peaks for Fe_2O_3-based materials (Fe_2O_3-Mor and Fe_2O_3-Spin) at approximately 1500 cm^{-1} and 1100 cm^{-1}. The slight difference in the C=O band positions may be due to the differences in the phytochemical compositions of the Moringa oleifera and Spinacia oleracea extracts used during synthesis. Furthermore, bands associated with C=O and C-N stretching vibrations are visible in the composite materials (Fe_2O_3-Pyrr-Mor and Fe_2O_3-Pyrr-Spin) at approximately 1500 cm^{-1} -1300 cm^{-1} range. This indicates the presence of the conjugated ring structure of polypyrrole, confirming that polymerization was successful. This assignment is further supported by the C-N stretching vibration also present in the pure polypyrrole at approximately 1331.07 cm^{-1}. Furthermore, both the composite materials and pure polypyrrole show additional peaks in the range of approximately 1200-1000 cm^{-1}, which are due to the C-H in-plane bending vibrations of polypyrrole as well as general C-H bending vibrations. The strong vibration bands seen at the 500 cm^{-1}-400 cm^{-1} region correspond to Fe-O vibrations, confirming the presence of the Fe_2O_3 crystalline core in both the nanoparticles and their composite materials, indicating that the core structure remains unaffected after incorporation of polypyrrole. The additional peaks seen in the composite materials and pure polypyrrole may also be associated with impurities or S-O stretching vibrations from the initiator, which typically appear in the 1300-1000 cm^{-1} and 700-600 cm^{-1} regions [8], [41], [17].

4.3. NiO Nanoparticles and their Composites

Figure 11 depicts the FTIR of the synthesized NiO nanoparticles, their polypyrrole-based composites, and pure polypyrrole obtained in the wavenumber range of 400-4000 cm^{-1}. Similar to the Fe_2O_3-based materials, an

absorption band at approximately 3300 cm^{-1} is seen and is assigned to O-H stretching vibrations. This band is more intense in the composite materials compared to the pure NiO nanoparticles, which can be due to the overlap of O-H stretching vibrations from surface adsorbed water and the N-H stretching vibrations associated with polypyrrole. The presence of adsorbed water is further indicated by the absorption band at approximately 1500 cm^{-1} in the pure NiO nanoparticles, which are assigned to the H-O-H bending vibration. Furthermore, the O-C=O symmetric and asymmetric stretching vibration and C-O stretching vibration resulting from adsorption of the surrounding atmosphere are responsible for the peaks found at the range 1300-1200 cm^{-1}. In the composite material, the C=O and C-N stretching vibrations at approximately 1500 cm^{-1} corresponds to fundamental vibrations of the polypyrrole ring and suggests successful polymerization. Additionally, the bands at the 1300-1000 cm^{-1} region are assigned to C-H in-plane bending vibrations of polypyrrole. Lastly, the NiO vibration is represented by a weak absorption band in the range at approximately 500-400 cm^{-1}, which are seen in both the pure NiO nanoparticles and their composite materials. This shows that the NiO crystalline structure is maintained after composite formation and indicates the nanoparticles successful synthesis [2,14,40].

4.4. Polypyrrole

The FTIR spectra of pure polypyrrole obtained between 4000-400 cm^{-1} is shown in both Figure 10 and Figure 11. The N-H symmetric stretching of vibration is responsible for the band at 3203.59 cm^{-1}. The band at approximately 1650 cm-1 is assigned to C=O stretching vibration. In the area of 1592.47 cm^{-1}, the stretching of C=C within the polymer became visible. The ring stretching and C-N vibrations are seen at 1331.07 cm^{-1}. Pyrrole ring and out-of-plane C-H bending are the causes of the band in the 1050 -900 cm^{-1} region. The bands found in this spectrum are consistent with those found in the scientific literature and confirm that the polymerization of pyrrole [37].

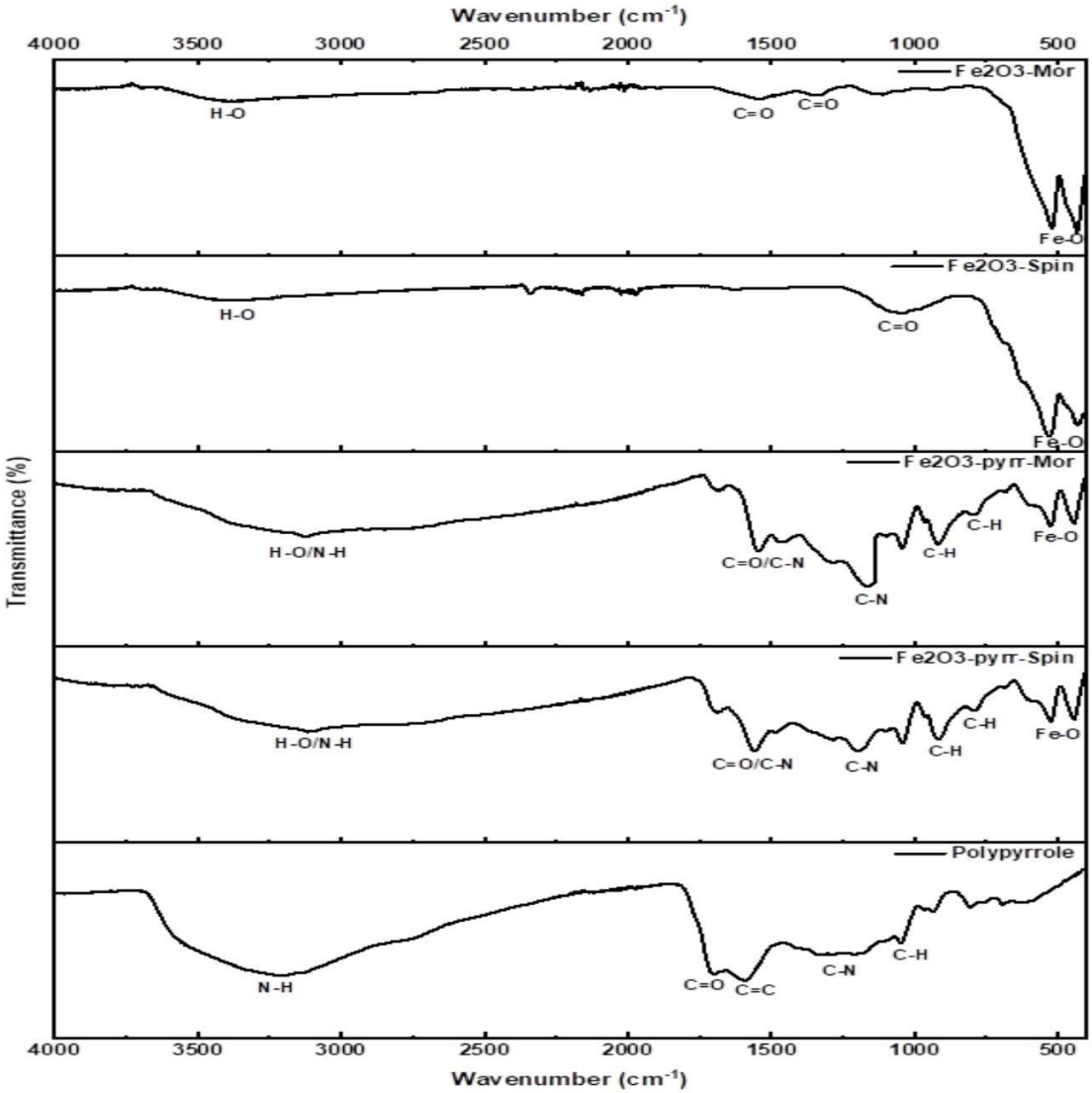

Figure 10: FTIR spectra of Fe_2O_3 nanoparticles and their polypyrrole-based composite materials synthesized using plant extract from *Moringa oleifera* and *Spinacia oleracea,* along with polypyrrole

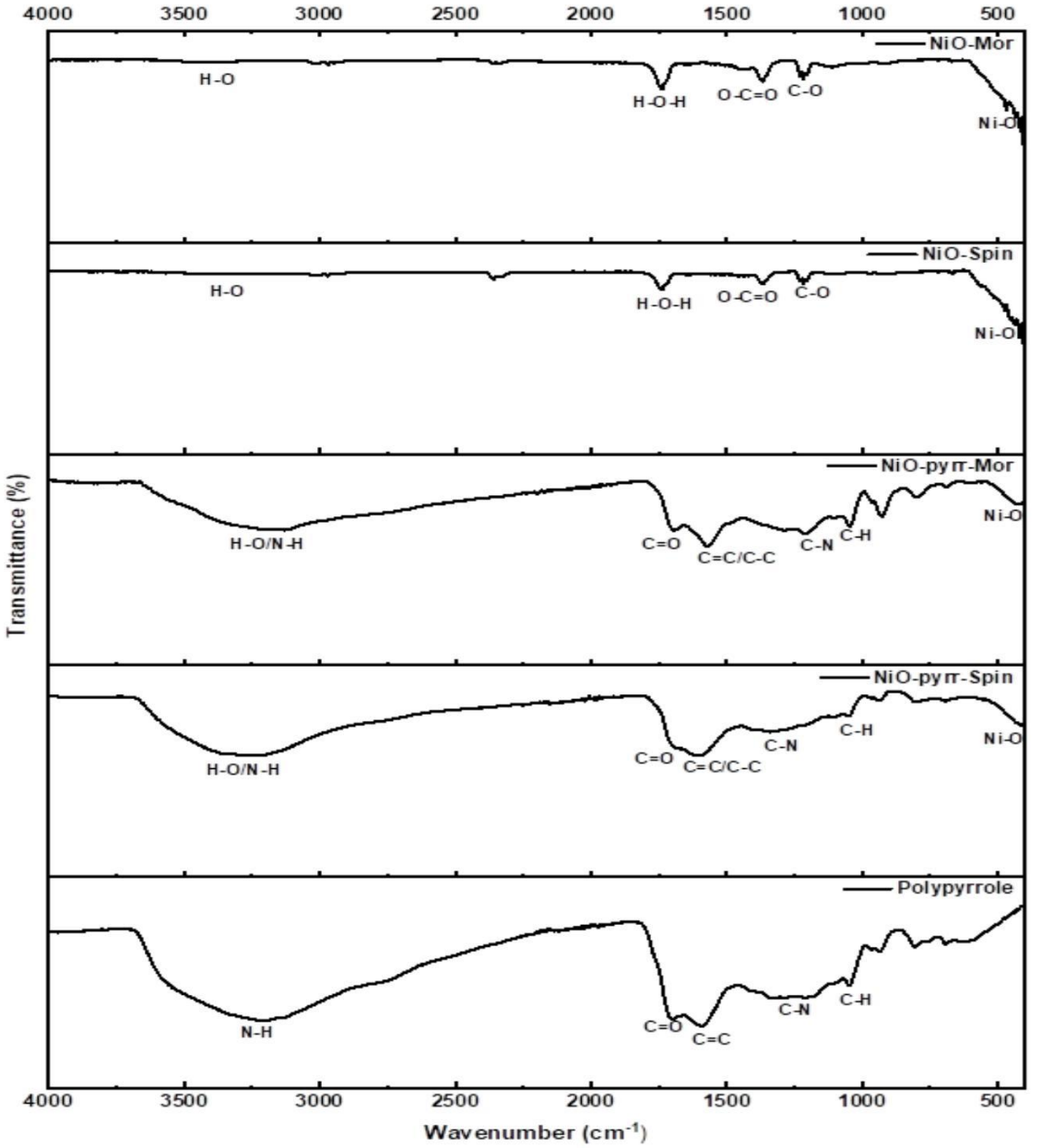

Figure 11: FTIR spectra of NiO nanoparticles and their polypyrrole-based composite materials synthesized using plant extract from *Moringa oleifera* and *Spinacia oleracea*, along with polypyrrole

4.5. Structural Characterization (XRD)

XRD at 40 kV was used to identify crystalline phases and to estimate the crystalline sizes.

4.6. XRD of Fe_2O_3 and it's Composite

The XRD patterns of the synthesized Fe_2O_3 nanoparticles, their polypyrrole-based composites, and pure polypyrrole are shown in Figure 12. The diffraction patterns of the Fe_2O_3 nanoparticles and their composites are similar, which shows that the formation of the composite did not change the crystalline structure of Fe_2O_3. XRD analysis of the nanoparticles and their composites shows well defined Bragg reflection characteristics of Fe_2O_3. The diffraction peaks at 2θ = 25.05°, 33.84°, 36.42°, 41.86°, 50.02°, 54.61°, 63.45°, 64.23° and 73.52° can be indexed to the (012), (104), (110), (113), (024), (116), (018), (214) and (300) planes, respectively. The most prominent peaks at 33 and 36 degrees correspond to the (104) and (110) planes, respectively, confirming the formation of α-Fe_2O_3 phase. Furthermore, every diffraction peak in the XRD pattern can be linked to the standard data for α-Fe_2O_3 rhombohedral (trigonal) crystal structure with space group R-3c (COD ID:1011240), confirming the phase purity and effective synthesis of α-Fe_2O_3.

Additionally, the following Scherrer's equation was used to determine the average crystalline size of the Fe_2O_3 nanoparticles and their composites:

$$D=K\lambda/\beta\cos\theta \quad \ldots (1)$$

Where D is the crystalline size (nm), K is the shape factor 0.9, λ is the incident wavelength (nm), β is the full width at half maximum (FWHM), and θ is the facet's peak location [38]. The average crystallite size of the Fe_2O_3 nanoparticles synthesized from moringa, Fe_2O_3 nanoparticles synthesized from spinach, and their composites were determined to be 39, 39, 24, and 18 nm, respectively, using the high-intensity peaks (104) and (110), as indicated in Table 1. The Fe_2O_3 nanoparticles' crystalline size is significantly larger than that of their composite materials. This is because the pure Fe_2O_3 nanoparticles have well-defined and sharp diffraction peaks, which indicate better crystallinity, while the composite materials crystallinity was reduced by the addition of pyrrole. The material is nanocrystalline according to the XRD's strong peaks and particle size of less than 100nm.

4.7. XRD of NiO and its Composites

Figure 13 shows the XRD patterns of the synthesized NiO nanoparticles, their composites, and polypyrrole. The peaks at 2θ = 37°, 43°, 62°, 76° and 79° correspond to the NiO crystal planes (111), (200), (220), (311), and [222], respectively. The diffraction peaks align with the face-centered cubic (FCC) crystalline structure (space group Fm-3m) of NiO, both in peak location and relative intensity. This is consistent with the standard spectrum (COD ID:1010093). Additionally, it is evident that the formation of the composite material does not change the crystalline structure of the NiO nanoparticles because there are no changes in their diffraction patterns. The high phase purity of the synthesized NiO nanoparticles was confirmed by the absence of additional diffraction peaks.

The average crystalline size of the NiO nanoparticles and their composite materials were also determined using the Scherrer's equation (Eq.1). The average crystalline size of the NiO nanoparticles synthesized from Moringa, NiO nanoparticles synthesized from spinach, and their composites were determined to be 16, 20, 11, and 12 nm, respectively, using the high-intensity peaks (111) and (200), as indicated in Table 2. The NiO nanoparticles crystalline size is significantly greater than that of their composite materials, confirming that the addition of pyrrole does decrease the crystalline size (AJC-25-Supplementary+Issue-41, n.d.). This is due to pyrrole's growth-inhibiting and capping properties, that increases nucleation density and restrict crystal growth, resulting in smaller crystallines [1].

4.8. Effect of the Addition of Pyrrole

When comparing the XRD patterns of the nanoparticles (Fe_2O_3 and NiO) to those of their composite materials (Fe_2O_3-pyrrole & NiO-pyrrole), the peak positions are identical, meaning that the polypyrrole's incorporation did not affect the crystalline material's lattice spacing. However, the overall intensity of the sharp crystalline peaks in the nanocomposites has decreased. The presence of polypyrrole, which is mostly amorphous and thus produce a broad, low intensity background rather than distinct diffraction peaks, is the reason for the decrease in intensity. This is because less of the X-ray beam is diffracted by the structured crystalline [32]. Additionally, no impurity phase peaks were found, suggesting that the products are pure phase.

Sample	2θ	Θ	FWHM	FWHM Corrected with 27°	D (nm)
Fe2O3 Moringa	33.12	0.28902652	0.2208	0.2106	39
Fe2O3 Spinach	33.02	0.28815386	0.22473	0.2148	39
Fe2O3-pyrrole Moringa	33.2	0.289637	0.3514	0.3451	24
Fe2O3-pyrrole Spinach	35.32	0.308225	0.4723	0.4676	18

Table 1: Depicts the Crystalline Size of the Fe_2O_3-Based Materials Calculated using High Intensity Peaks

Citation: Mkhonza, T.N., Nkabit , L.L. (2026). Preparat on of Fe_2O_3-Polypyrrole and NiO- Polypyrrole Nanocomposite Materials for the Photocatalyt i Generat i n of Hydrogen. *Int J Mater Sci, 2*(2), 1-23.

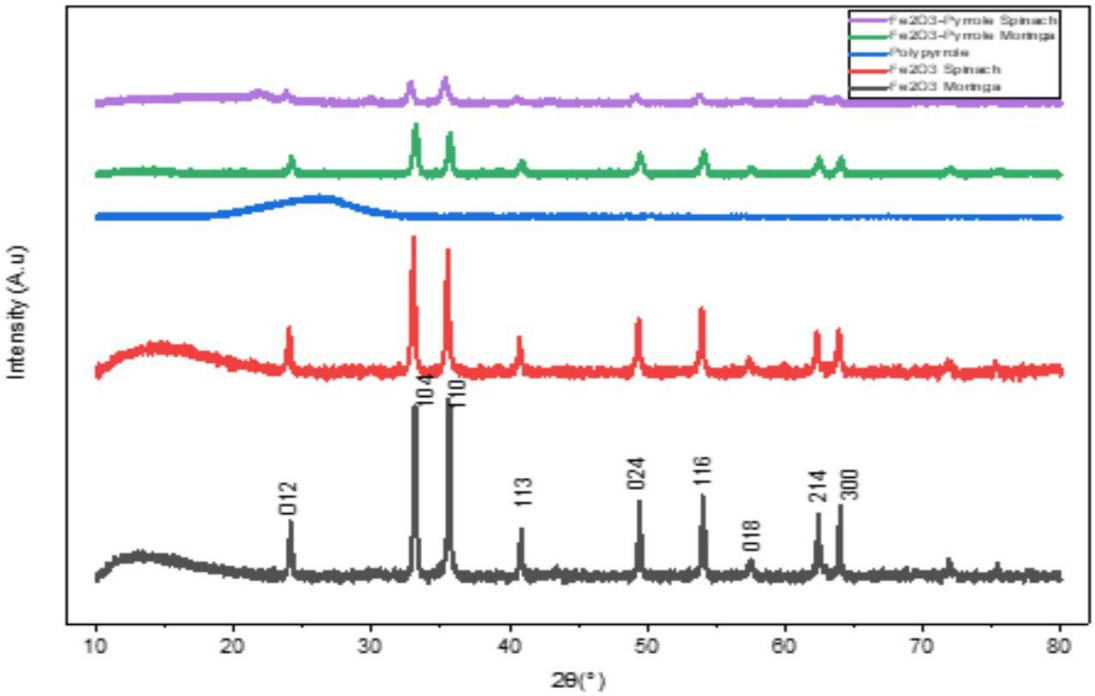

Figure 12: XRD Spectra of the Fe_2O_3-nanoparticle, their polypyrrole based composite materials and pure polypyrrole.

Sample	2θ	Θ	FWHM	FWHM Corrected with 27°	D (nm)
NiO Moringa	36.90	0.32218778	0.5148	0.5105	16
NiO Spinach	37.07	0.32349678	0.4256	0.4204	20
NiO-pyrrole Moringa	43.20	0.377253	0.8051	0.8024	11
NiO-pyrrole Spinach	43.05	0.375682	0.6957	0.6925	12

Table 2: Depicts the Crystalline Size of the NiO-based Material Calculated Using High Intensity Peaks

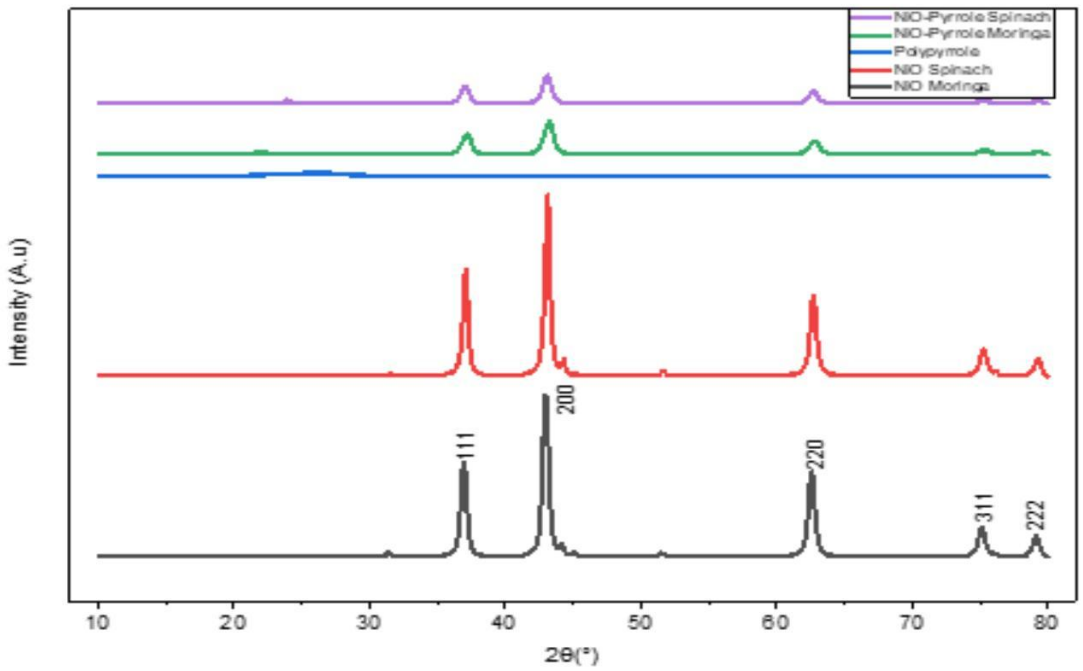

Figure 13: XRD Spectra of the NiO-Nanoparticle, their Polypyrrole Based Composite Materials and Pure Polypyrrole

4.9. Morphological Characterization (SEM & Particle size distribution)

4.9.1. SEM

The SEM images of the Fe_2O_3 and NiO nanoparticles synthesized from *Moringa oleifera* and *Spinacia oleracea* extract are shown in Figure 14 and Figure 16 at 10 µm and 100 nm, respectively. The SEM images of the nanocomposites of the synthesized nanoparticles are shown in Figure 15 and Figure 17 at 10 µm and 100 nm, respectively. Lastly, the SEM images of polypyrrole at 10 µm and 100 nm are shown in Figure 18.

In Figure 14, the Fe_2O_3 and NiO-based nanoparticles can be seen as big, stone-like clustered particles with a compact morphology, indicating a relatively low surface area. This suggests that they are highly agglomerated, resulting in uneven blocks that have little porosity. Whereas the composites of the nanoparticles (Figure 15) show noticeable morphological changes compared to the morphology of the oxide nanoparticles, they are more interconnected, more porous, and have less pronounced stone-like blocks. This means that the addition of polypyrrole changed the morphology by preventing extensive clustering. Additionally, pure polypyrrole shows a powder-like morphology in the 10-µm image, Figure 18. A comparatively large surface area is also indicated by the composite nanoparticles in Figure 15, which are scattered throughout this powder-like polypyrrole matrix. This implies that there will be more active sites where photocatalytic reactions can occur in the composite materials compared to the pure nanoparticles, and that the particles will be better exposed to light, increasing photocatalytic activation.

Figure 16 shows the high magnification of Fe_2O_3 and NiO-based nanoparticles at 100 nm. It is also evident that the aggregates discussed in Figure 14 are made up of irregular, roughly spherical nanoparticles with non-uniform sizes. Additionally, the nanoparticles formed from moringa look larger and more complex, suggesting less regulated growth, whereas the nanoparticles synthesized from spinach show smaller and better-defined spheres. The distinct spherical oxide nanoparticles are embedded in a continuous polypyrrole matrix, as seen in Figure 17, and their agglomeration is significantly lower than that of the oxide nanoparticles (Figure 16). Additionally, Figure 17 shows that the NiO polypyrrole-based composites have a larger surface area than the Fe_2O_3 polypyrrole-based composites. This is confirmed by the fact that the NiO composites show smaller, more evenly distributed nanoparticles with a more open structure, suggesting more porosity, whereas the Fe_2O_3 polypyrrole-based composites have more compact morphology suggesting lower porosity.

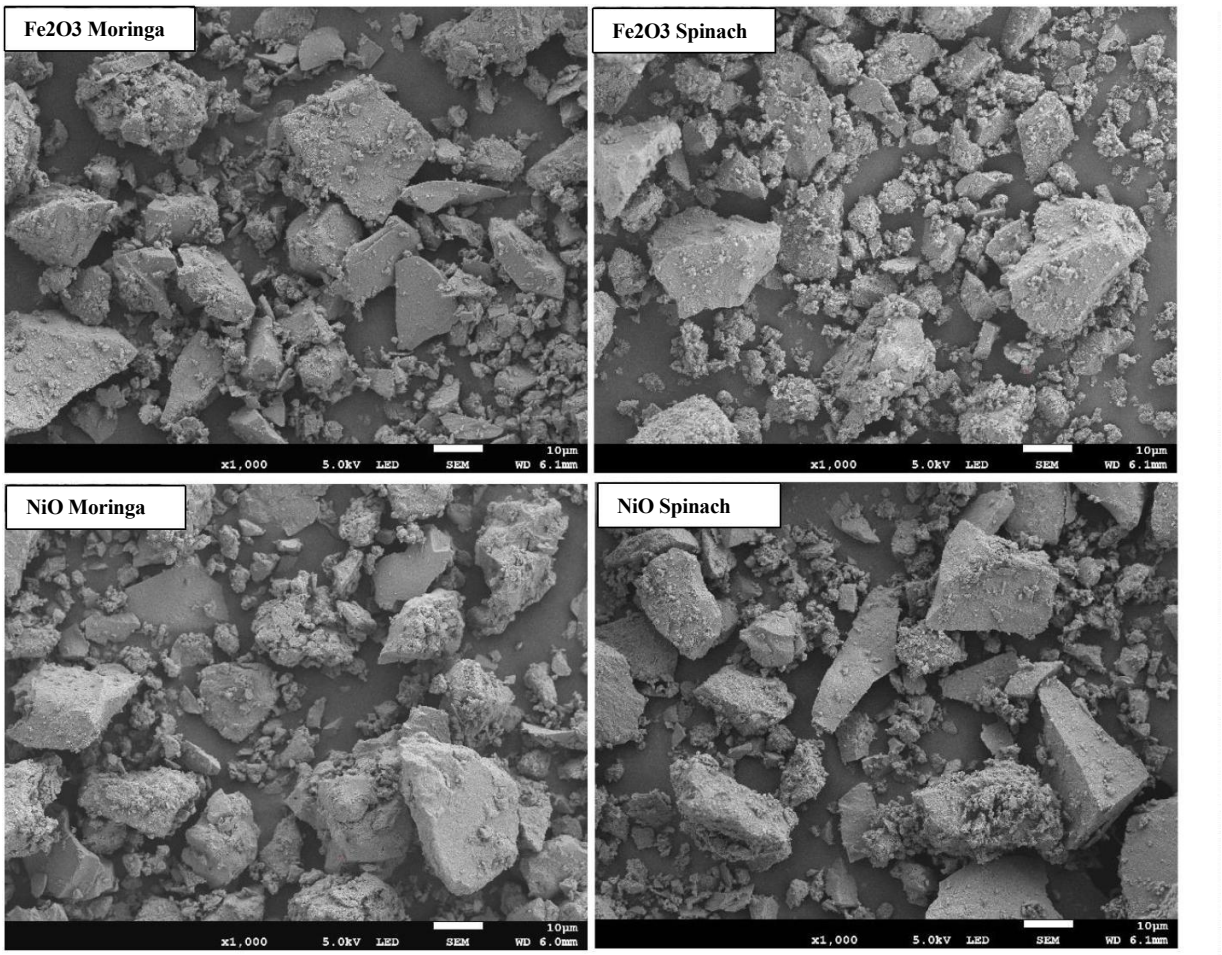

Figure 14: SEM showing (A) Fe_2O_3-Moringa, (B) Fe_2O_3-Spinach, (C) NiO-Moringa and (D) NiO-Spinach

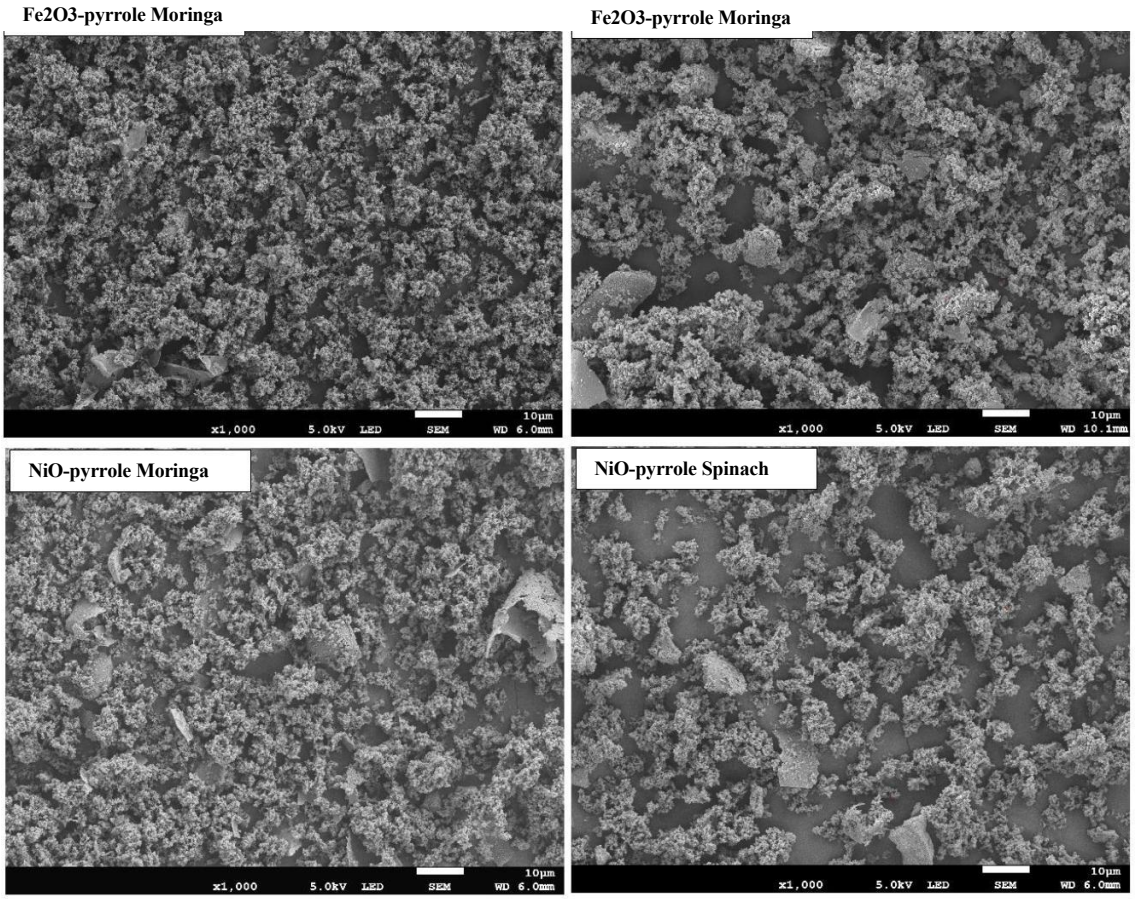

Figure 15: SEM Showing (A) Fe_2O_3-Pyrrole-Moringa, (B) Fe_2O_3- Pyrrole-Spinach, (C) NiO- Pyrrole-Moringa and (D) NiO- Pyrrole-Spinach Composites

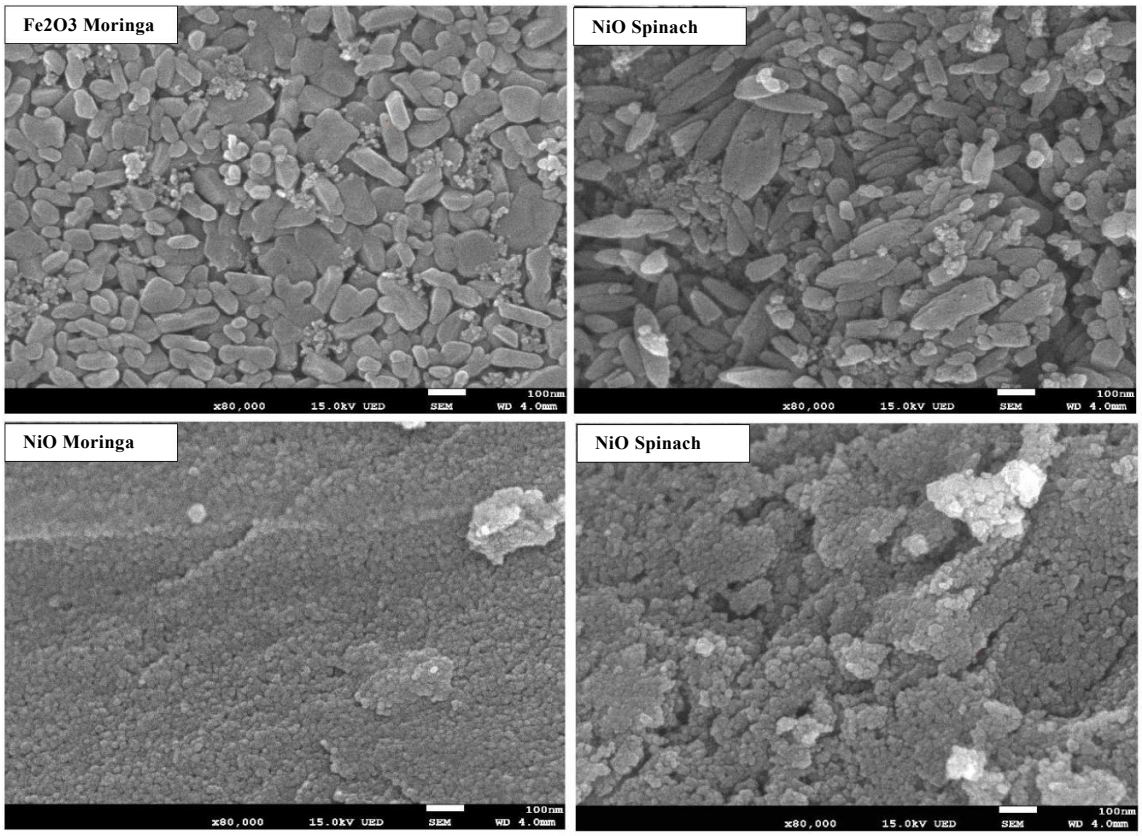

Figure 16: SEM Showing (A) Fe2O3-Moringa, (B) Fe_2O_3-Spinach, (C) NiO-Moringa and (D) NiO-Spinach Nanoparticles

Citation: Mkhonza, T.N., Nkabit , L.L. (2026). Preparat on of Fe_2O_3-Polypyrrole and NiO- Polypyrrole Nanocomposite Materials for the Photocatalyt i Generat i n of Hydrogen. *Int J Mater Sci, 2*(2), 1-23.

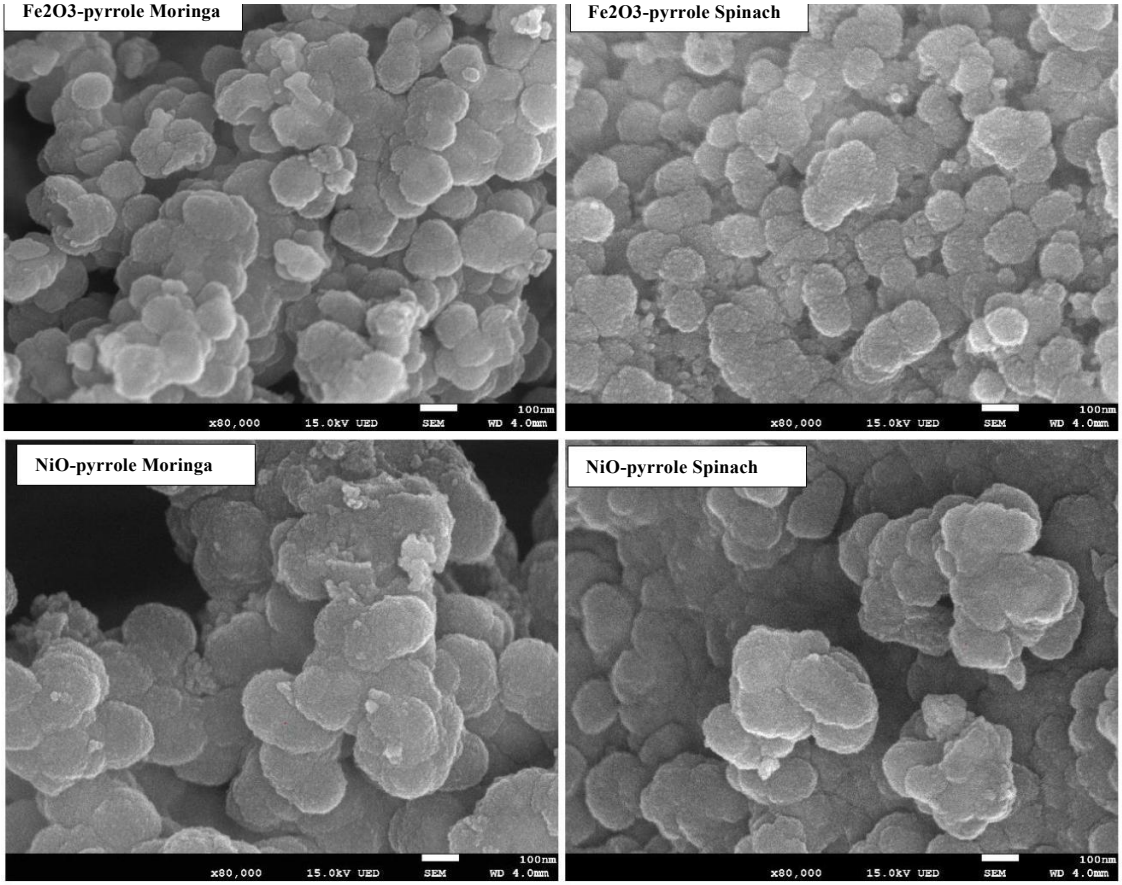

Figure 17: SEM Showing (A) Fe_2O_3- Pyrrole-Moringa, (B) Fe_2O_3- Pyrrole-Spinach, (C) NiO- Pyrrole-Moringa and (D) NiO- Pyrrole-Spinach Composites

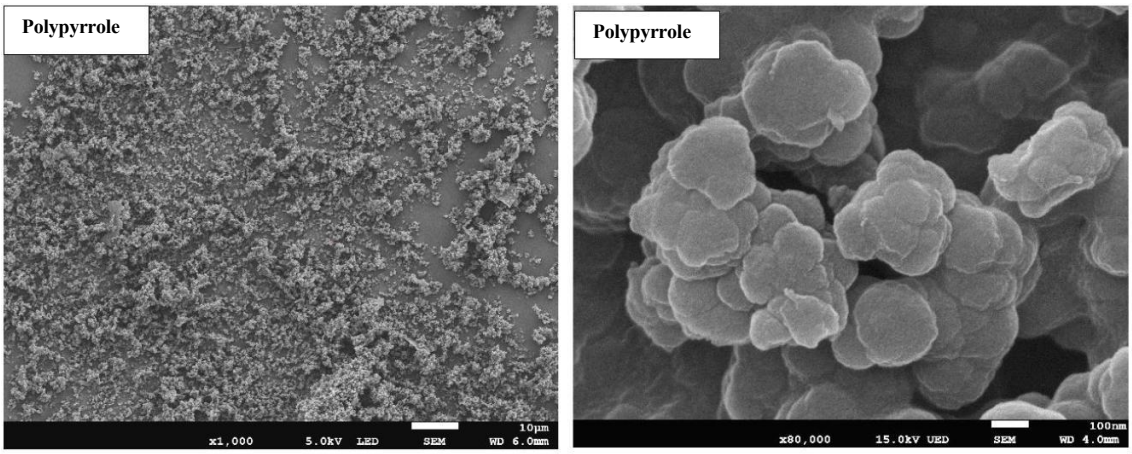

Figure 18: SEM Showing (A) Polypyrrole, (B) Polypyrrole at 100 nm

4.9.2. Particle Size Distribution

The average particle size of the synthesized nanoparticles, their composites, and polypyrrole was determined using the imageJ program. The average particle size was determined using SEM images obtained at 100 nm, which corresponds to Figure 16, 17, and 18. As shown in Figure 19, 20, and 21, a normal function was used to fit the particle size distribution in order to get the average particle size. The average size of the Fe_2O_3-moringa, Fe_2O_3-Spinach, Fe_2O_3-pyrrole-Moringa and Fe2O3-pyrrole-Spinach nanoparticles (Figure 19) were found to be 58.16, 26.39, 78.96 and 92.67 nm, respectively. The average size of the NiO-Moringa, NiO-Spinach, NiO-pyrrole-Moringa and NiO-pyrrole-Spinach nanoparticles (Figure 20) were found to be 21.84, 19.13, 125.27 and 90.82 nm, respectively. Lastly, the average particle size of polypyrrole (Figure 21) was found to be 79.95 nm.

The average particle size of all the synthesized samples falls within the nanometer range (< 100nm for majority of the particles) meeting the criteria for nanoparticles. The

polymer coating by polypyrrole, which raises the effective particle size, are the reason why it is evident that the composite materials are significantly larger than the pure nanoparticle samples.

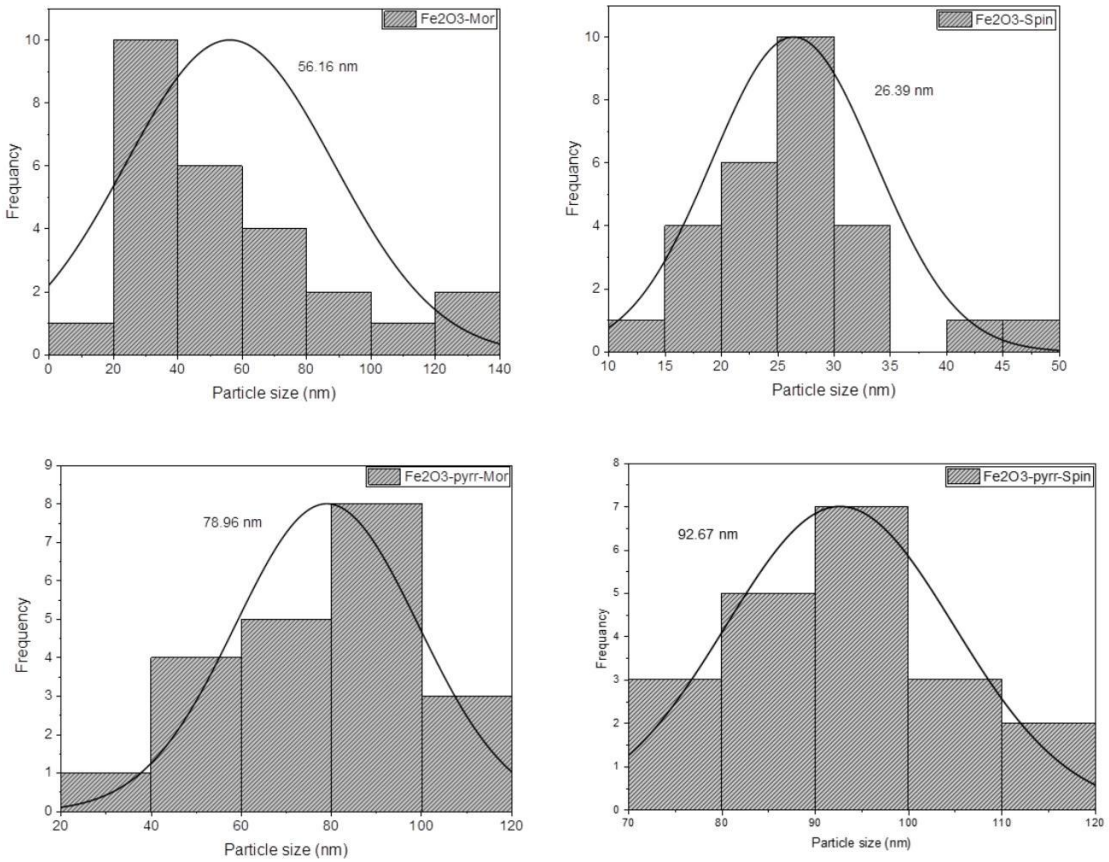

Figure 19: Particles Size Distribution of Fe_2O_3-Moringa, Fe_2O_3-Spinach, Fe_2O_3-pyrr-Moring and Fe_2O_3-pyrr-Spinach

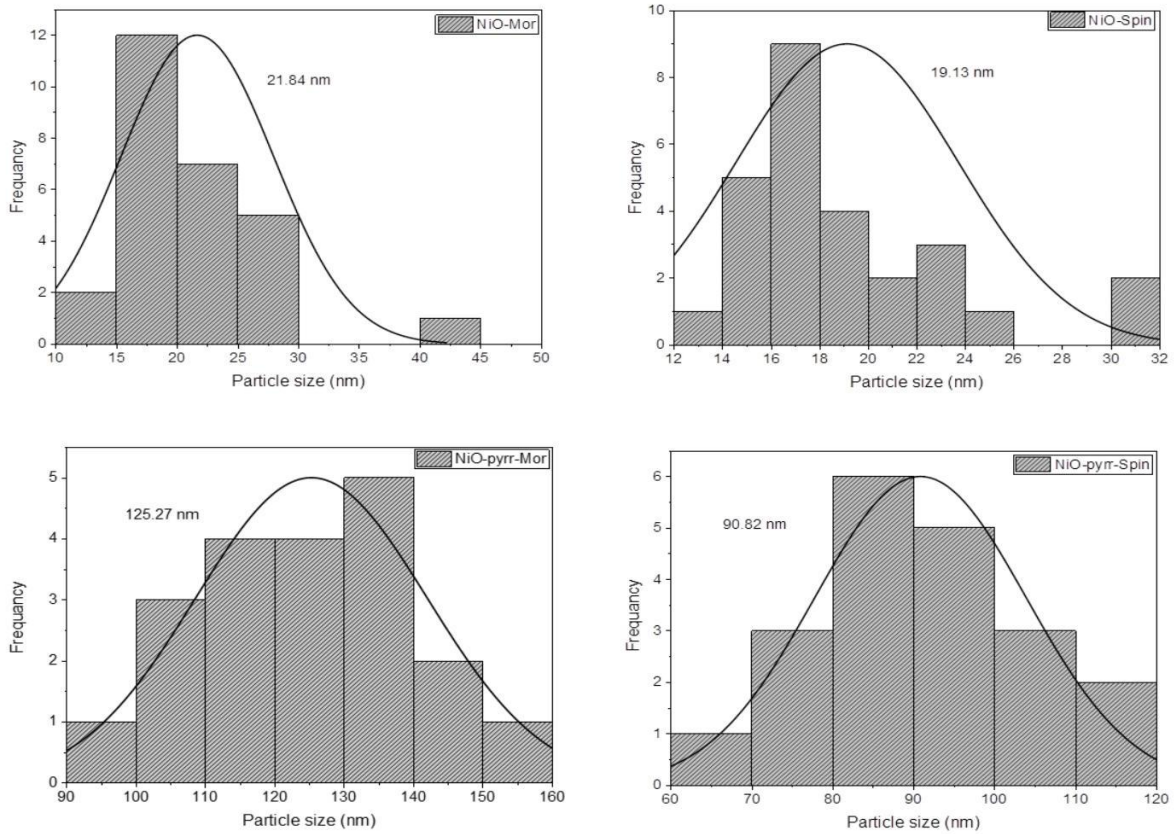

Figure 20: Particles Size Distribution of NiO-Moringa, NiO-spinach, NiO-pyrr-Moring and NiO-pyrr-Spinach

Citation: Mkhonza, T.N., Nkabit , L.L. (2026). Preparat on of Fe_2O_3-Polypyrrole and NiO- Polypyrrole Nanocomposite Materials for the Photocatalyt i Generat i n of Hydrogen. *Int J Mater Sci, 2*(2), 1-23.

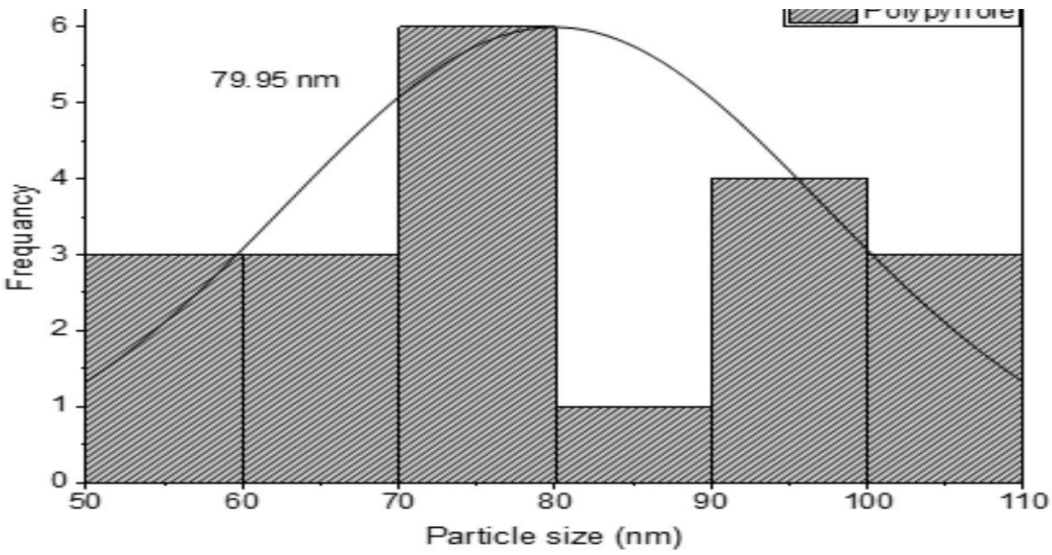

Figure 21: Particles Size Distribution of Polypyrrole

4.10. Element Composition Analysis (EDS)

The material's chemical composition was determined under SEM using EDS. A carbon sample holder was used to analyze the samples. The EDS of Fe_2O_3 nanoparticles and their composite materials produced from Moringa or Spinach extract, is shown in Figure 22, confirming the presence of Fe and O with weight percent for both the pure Fe_2O_3 nanoparticles and its composite materials, an additional N and C element peaks on the nanocomposite materials are due to the addition of pyrrole. Even though the samples were thoroughly rinsed during centrifugation step, it is evident that the samples still contained peaks associated with the elements Cl, Na, and S.

Furthermore, when looking at the EDS of the NiO nanoparticles along with their composite materials shown in Figure 23, Ni and O peaks with weighed percents are present for both the pure NiO material and composite material, an additional N and C element peaks on the composite materials which confirms the successful incorporation of pyrrole. There are traces of Cl, Na and S elements that are also present in the samples, which are the traces from the starting material.

Lastly, the EDS of pure polypyrrole is shown in Figure 24, it is evidence that there is a weighed percent of peaks associated with C and N elements which confirms the polypyrroles backbone synthesis. The additional peaks associated with O, S and K are from the potassium persulfate that was used as an initiator for the polymerization process.

Additionally, the C element that can be seen in all the samples, NiO, Fe_2O_3, their composite materials and Polypyrrole may also be due to the presence of organic compounds that are present in the plant extracts that were used for the synthesis or sample holder used during SEM analysis. The reason the Ir element is present in every sample is because it was used to coat the samples prior to analysis.

Citation: Mkhonza, T.N., Nkabit , L.L. (2026). Preparat on of Fe_2O_3-Polypyrrole and NiO- Polypyrrole Nanocomposite Materials for the Photocatalyt i Generat i n of Hydrogen. *Int J Mater Sci, 2*(2), 1-23.

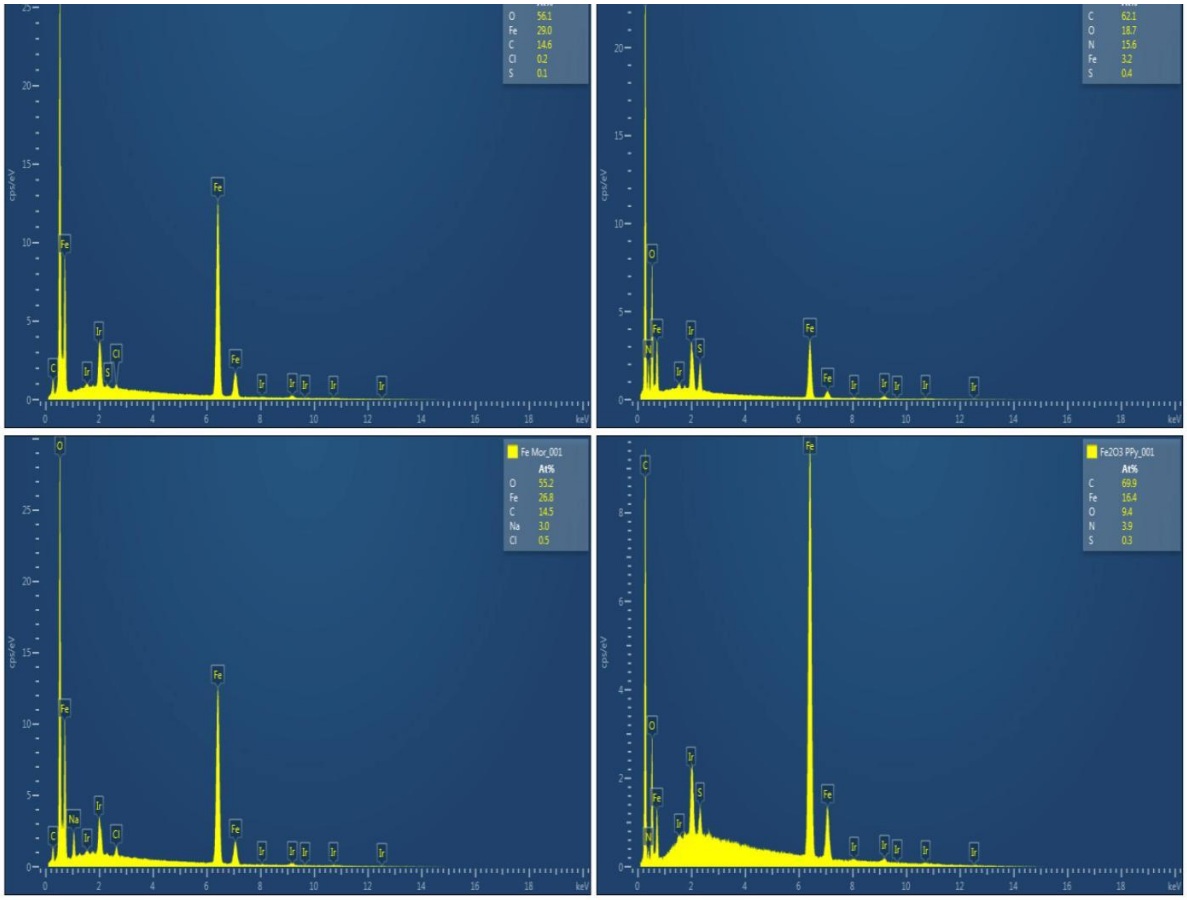

Figure 22: EDS spectrum of Fe_2O_3-Spin, Fe_2O_3-pyrr-Mor, Fe_2O_3-Mor, and Fe_2O_3-pyrr-Spin

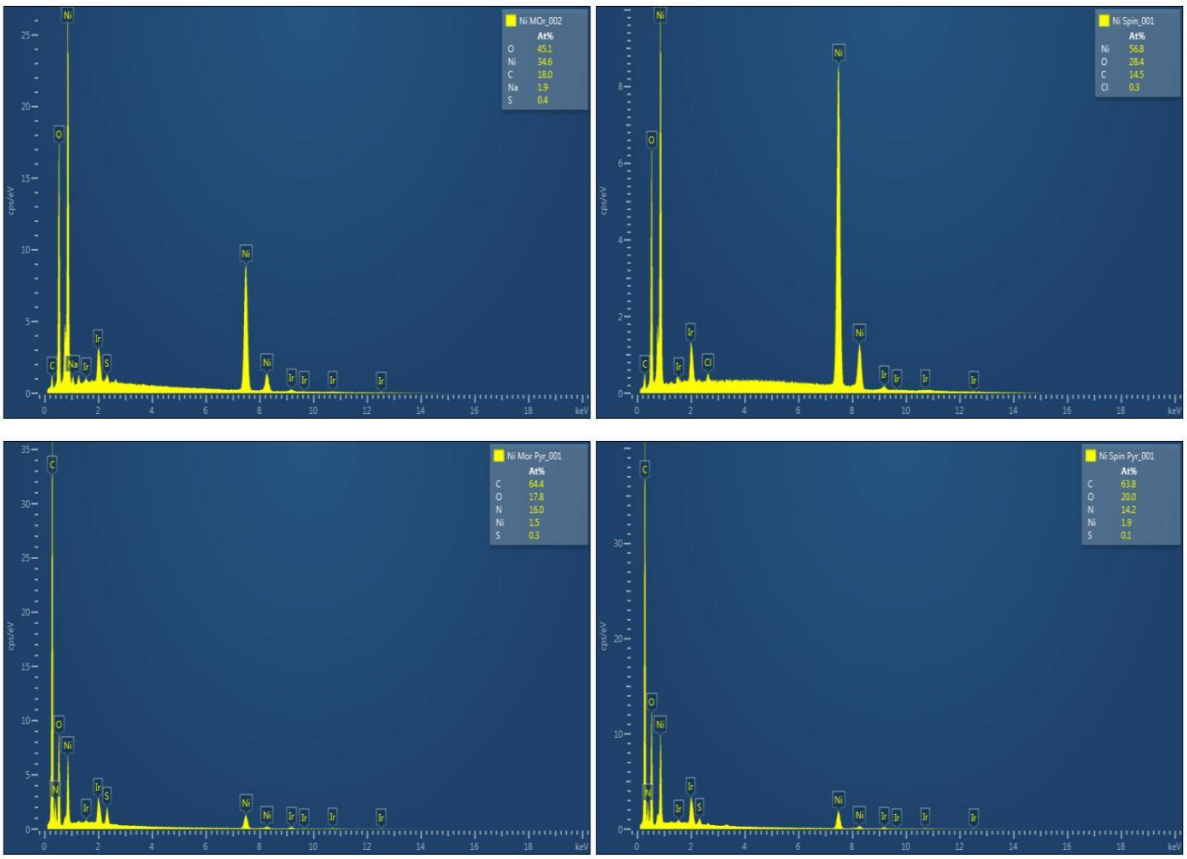

Figure 23: EDS Spectrum of NiO-Mor, NiO-Spin, NiO-pyrr-Mor, and Fe_2O_3-pyrr-Spin

Citation: Mkhonza, T.N., Nkabit , L.L. (2026). Preparat on of Fe_2O_3-Polypyrrole and NiO- Polypyrrole Nanocomposite Materials for the Photocatalyt i Generat i n of Hydrogen. *Int J Mater Sci, 2*(2), 1-23.

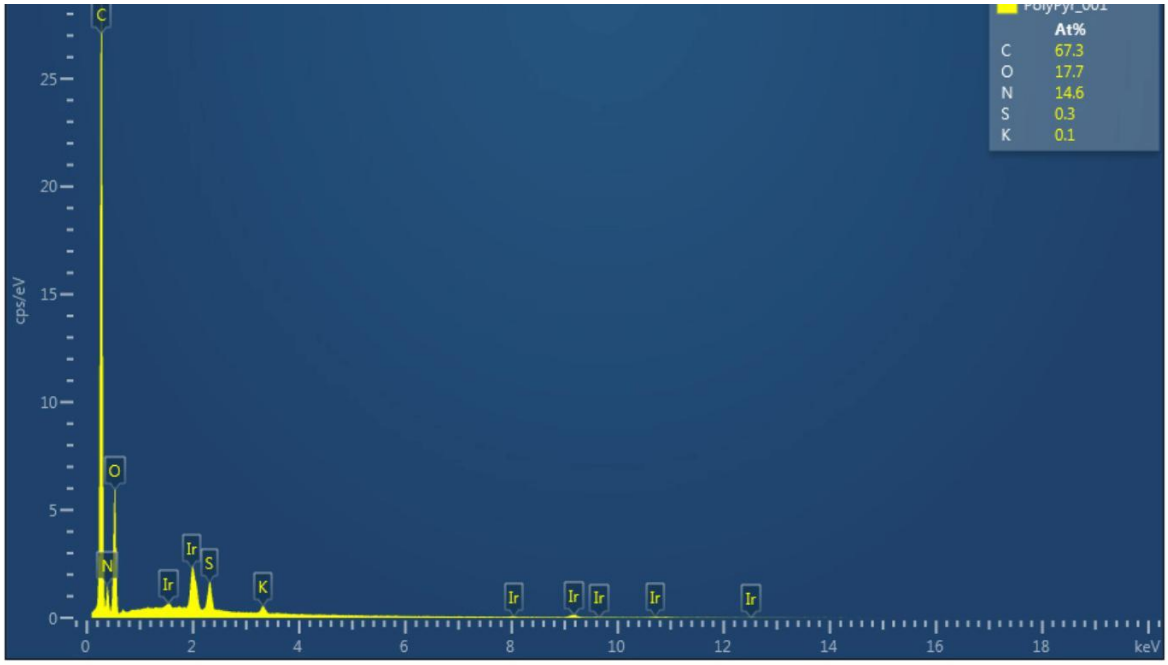

Figure 24: EDS Spectrum of Polypyrrole

Samples	*Element weight Percentage (%)*				
	F	Ni	O	N	C
Fe2O3-Mor	3.2	-	52.2	-	14.4
Fe2O3-Spin	29.0	-	56.1	-	14.6
Fe2O3-pyrr-Mor	26.8	-	18.7	15.6	62.1
Fe2O3-pyrr-Spin	16.4	-	9.4	3.9	69.9
NiO-Mor	-	34.6	45.1	-	18.0
NiO-Spin	-	56.8	28.4	-	14.5
NiO-pyrr-Mor	-	1.5	17.8	16.0	64.4
NiO-pyrr-Spin	-	1.9	20.0	14.2	63.8
Polypyrrole	-	-	17.7	14.6	67.3

Table 3: Element Weight Percentage of all the Synthesized Samples from EDS

4.11. Optical Characterization (UV-Vis Spectroscopy and Tauc Analysis)

Optical properties of the synthesized nanoparticles, their nanocomposite materials, and pure polypyrrole were determined through UV-Vis. The wavelength vs absorbance graphs were plotted from 250 nm -800nm. These plots were then used to estimate their energy band gap using the Tauc relation:

$$(ahv)^2 = b(hv - Eg)^n \quad ...2$$

Where a stands for absorption, h for Planks constant, v for frequency, b for constant, and *Eg* for the band gap in electrovolt (eV). Since the indirect transition was used in this instance, n = 2 [28].

The bandgap for Fe_2O_3-moringa, Fe_2O_3-Spinach, Fe_2O_3-pyr-moringa and Fe_2O_3-pyrr-spin are approximately 1.57, 1.48, 1.91 and 1.85 eV, respectively, according to Figure 25 and Figure 26. Semiconducting behaviour is indicated by bandgap values between 1 and 2 eV, which allow for the efficient absorption of visible light. As a result, it is expected that these nanoparticles and their nanocomposites will be suitable for photocatalytic applications driven by visible light [28].

Furthermore, the bandgap for NiO-moringa, NiO-Spinach, NiO-pyrr-moringa and NiO-pyrr-spin are approximately 2.63, 2.63,2.2 and 2.47 eV, respectively (as seen in Figure 27 and Figure 28). In comparison to the Fe_2O_3-based materials, the values show semiconductive behaviour with a larger bandgap, indicating decreased but still appreciable

absorption of visible light. The NiO-pyrrole composites have slightly lower bandgap compared to the pure NiO-based nanoparticles, this indicates that they have better light absorption, which could improve their photocatalytic efficiency.

Lastly, pure polypyrrole has a bandgap of approximately 3 eV, which is relatively high compared to the other synthesized nanoparticles. This high bandgap shows that pure polypyrrol has limited electrical conductivity. However, when polypyrrole is incorporated into a composite with other materials (as seen in Figure 26 and Figure 28), a small decrease in the bandgap is observed. This decrease suggests improved transport charges within the composite material. As a result, although polypyrrole is not a very conductive substance on its own, it improves the composites electrical conductivity when incorporated into the pure synthesized nanoparticles.

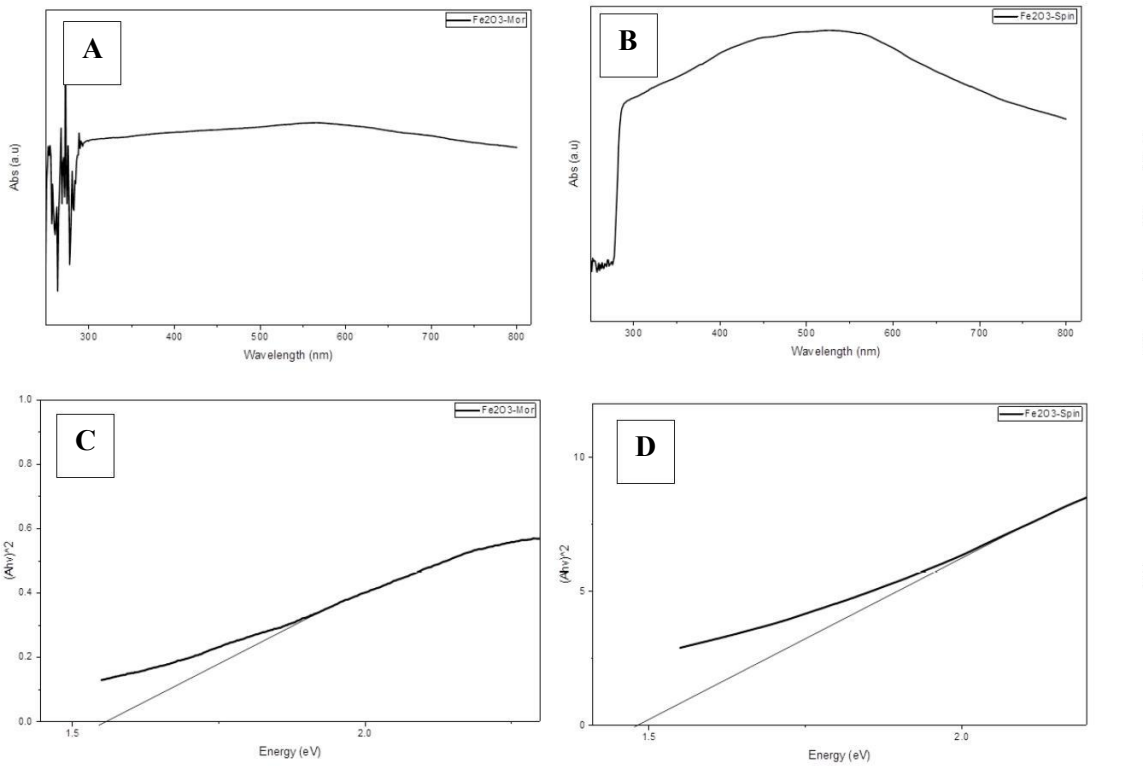

Figure 25: UV Spectrum and Tauc Plots Showing Indirect Energy Bandgap of Fe_2O_3-Mor and Fe_2O_3-Spin

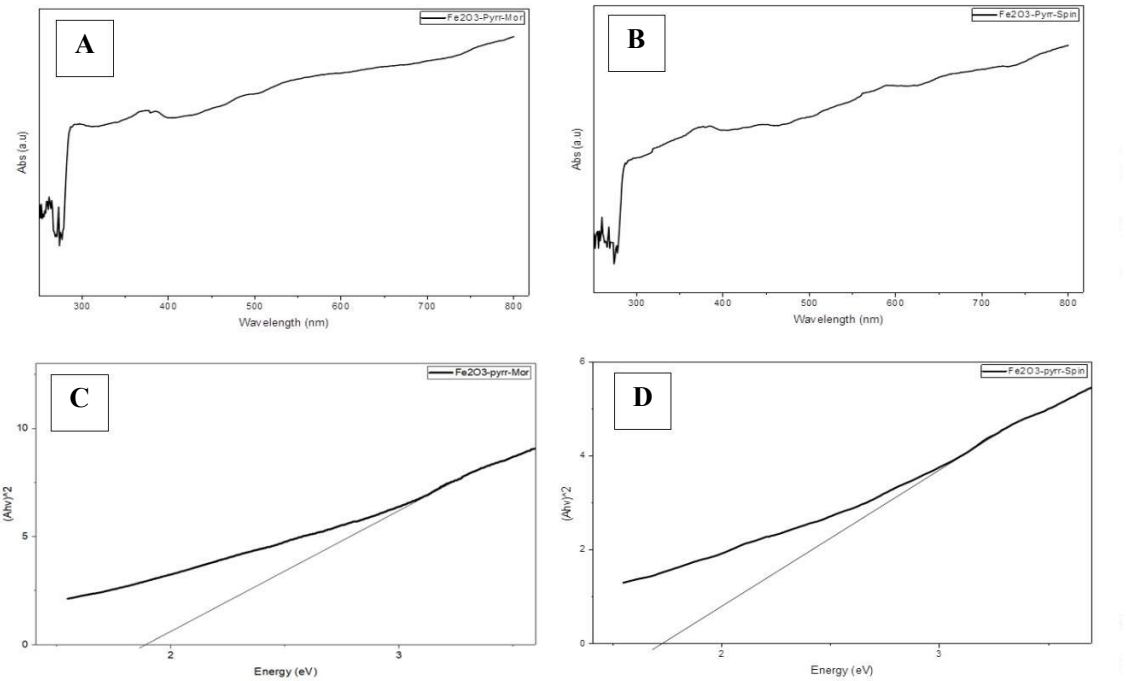

Figure 26: UV Spectrum and Tauc Plots Showing Indirect Energy Bandgap of Fe_2O_3-pyrr-Mor and Fe_2O_3-pyrr-Spin

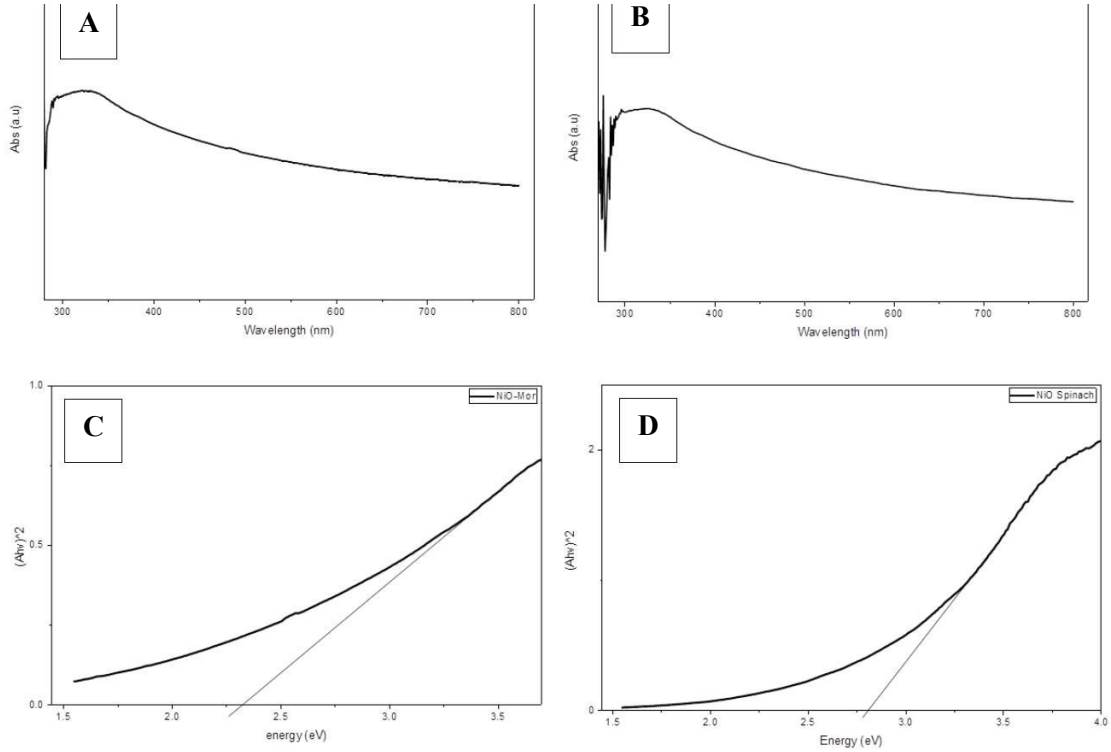

Figure 27: UV Spectrum and Tauc Plots Showing Indirect Energy Bandgap of NiO-Mor and NiO-Spin

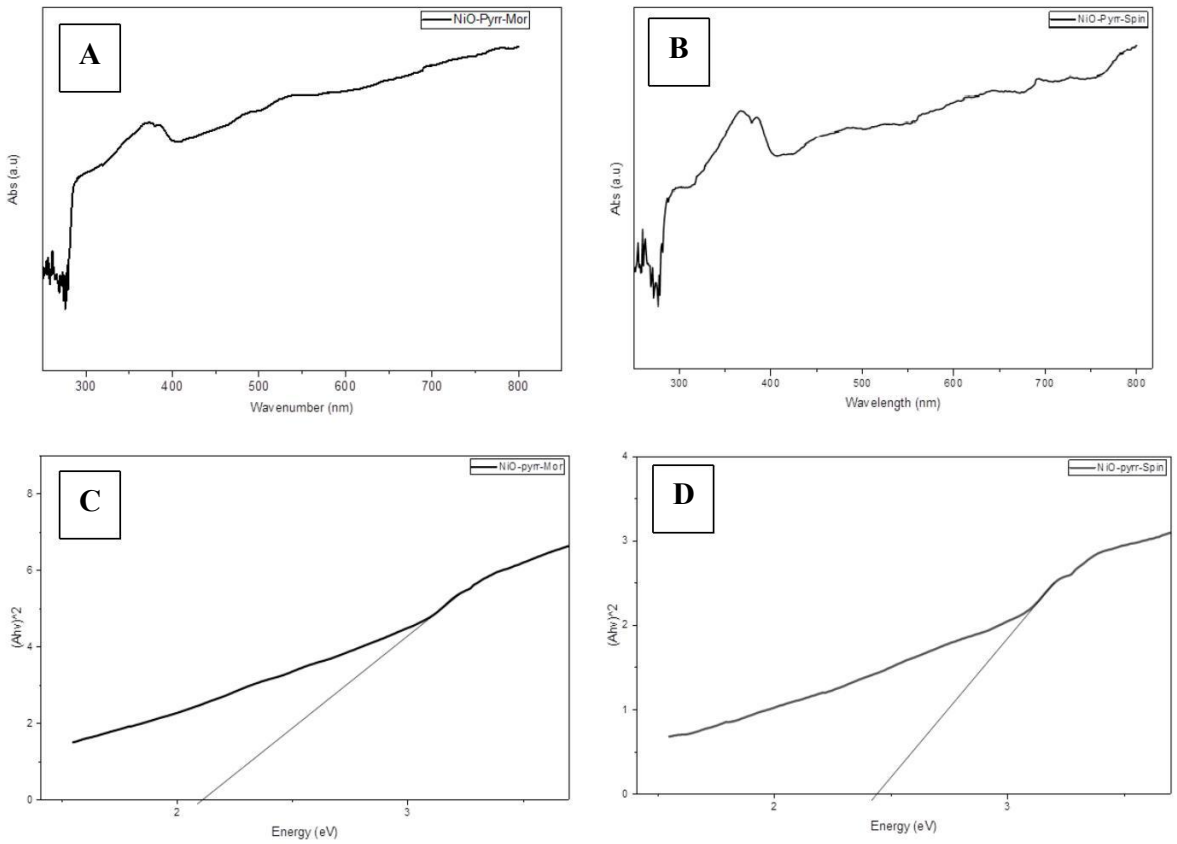

Figure 28: UV Spectrum and Tauc Plots Showing Indirect Energy Bandgap of NiO-Pyrrole-Moringa and NiO-Pyrrole-Spinach

4.12. Electrochemical Characterization (CV)

Figure 29, Figure 30 and Figure 31 show the cyclic voltammetry (CV) profiles of the Fe_2O_3 based nanoparticles, NiO based nanoparticles and the pure polypyrrole, respectively. The measurements were conducted in a three-electrode cell using a glassy carbon electrode, a Pt wire counter electrode and an Ag/AgCl reference electrode in 3M NaCl aqueous solution. For each sample, the CV measurements were performed three times to ensure the repeatability and accuracy of the electrochemical results. The CV analysis was performed to assess the electrochemical behaviour and verify the electrical conductivity of the synthesized materials. The Potassium Ferrocynide redox couple ($K_4[Fe(CN)_6]$) was used as the bare reference system to record the cyclic voltammetry profiles.

Figure 29, Figure 30 and Figure 31 show that after the glassy carbon was coated with Fe_2O_3-based/NiO-based nanoparticles or pure polypyrrole, there was a noticeable increase in both cathodic and anodic peak currents when compared to the bare KFeCN. The increase in peak current shows a larger electroactive surface area after being coated, which provides more active site for the reaction. Furthermore, the modified electrodes show improved peak symmetry and reduced peak-to-peak separations (ΔE_p) compared to the bare, indicating increased electrochemical reversibility, quicker charge transfer and better conductivity.

The higher peak current and smaller peak separation in these CV results indicate the higher electrocatalytic activity and conductivity of these synthesized materials. The Fe_2O_3 and NiO nanoparticles enhance electron transport and contribute to pseudocapacitive behaviour, whereas the conjugated structure of polypyrrole facilitates easier electron mobility. These effects reduce energy losses during redox reactions and are significant for applications like hydrogen production and ammonia decomposition [12,28].

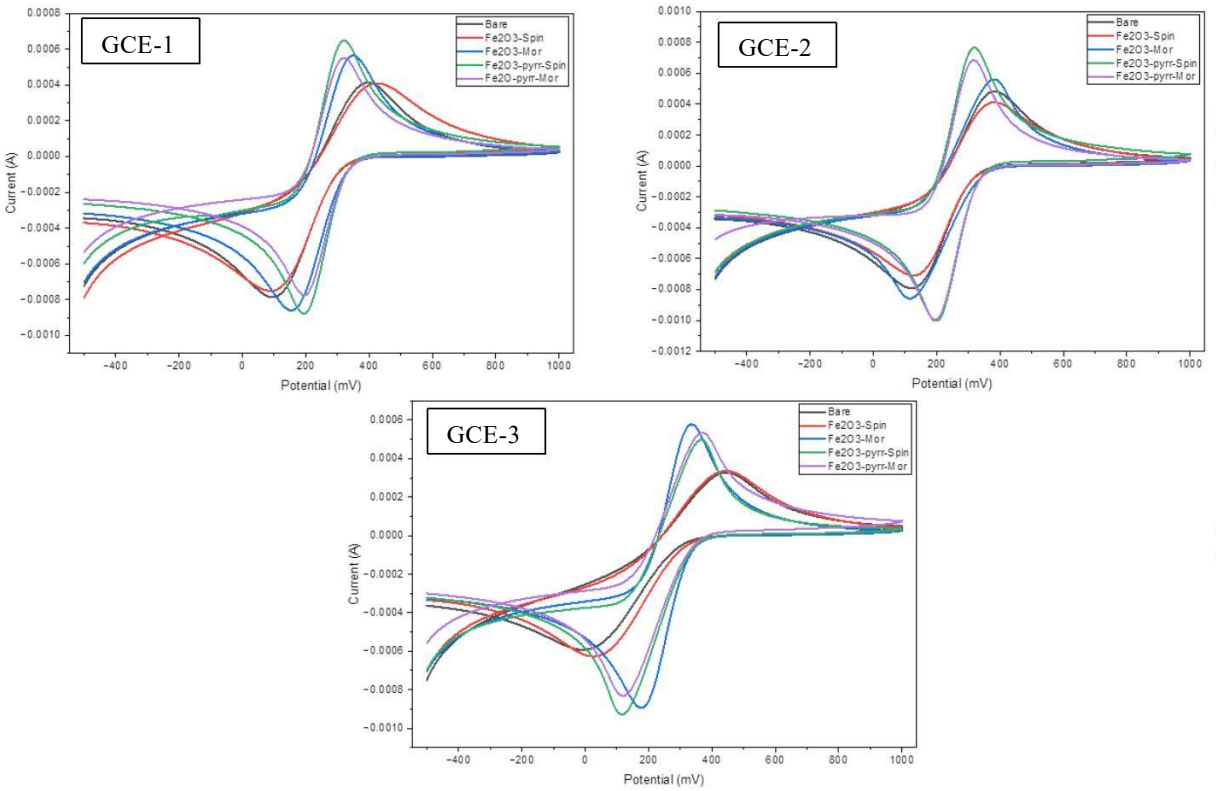

Figure 29: Cyclic voltammetry curves of the (KFeCN), Fe_2O_3-Spinach, Fe_2O_3-Moringa, Fe_2O_3-pyrrol-Mor and Fe_2O_3-pyrrole-Spinach obtained using three different glassy carbon electrodes

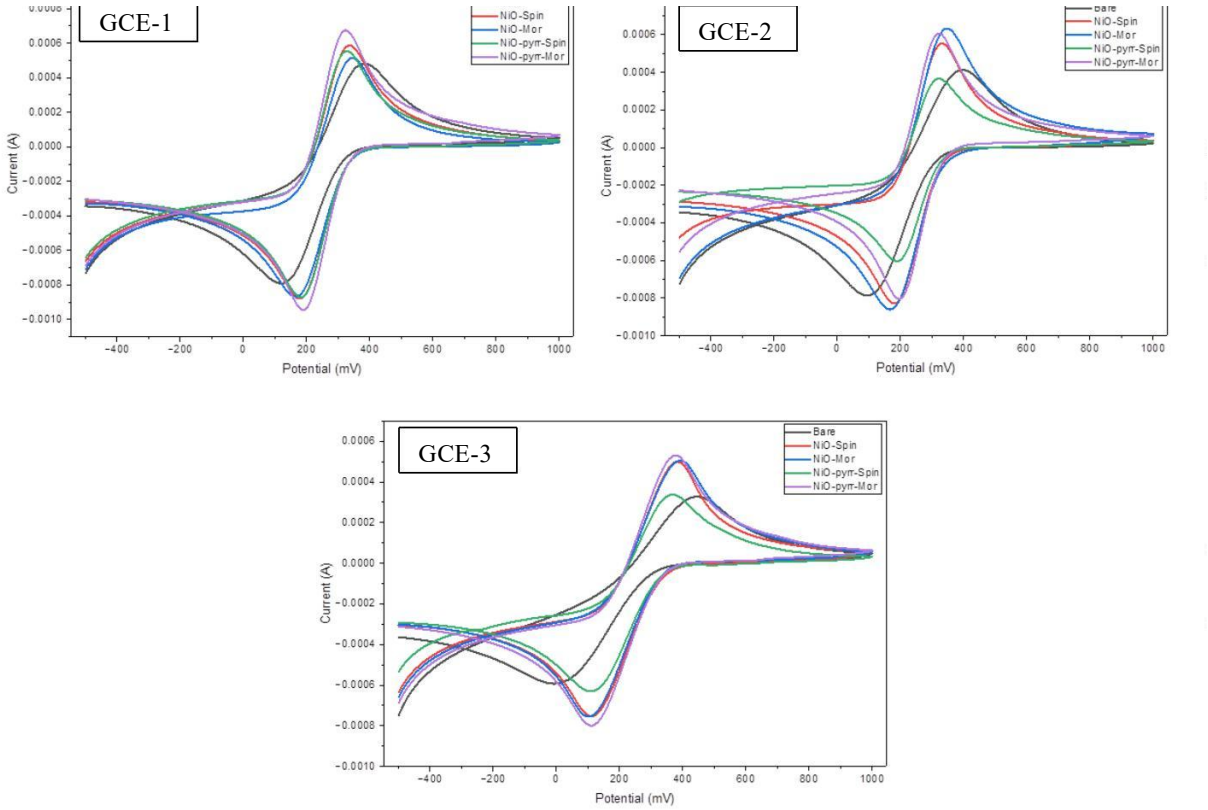

Figure 30: Cyclic Voltammetry Curves of the Bare (KFeCN), NiO-Spinach, Nio-Moringa, NiO-pyrrol-Mor and NiO-pyrrole-Spinach Obtained Using Three Different Glassy Carbon Electrodes

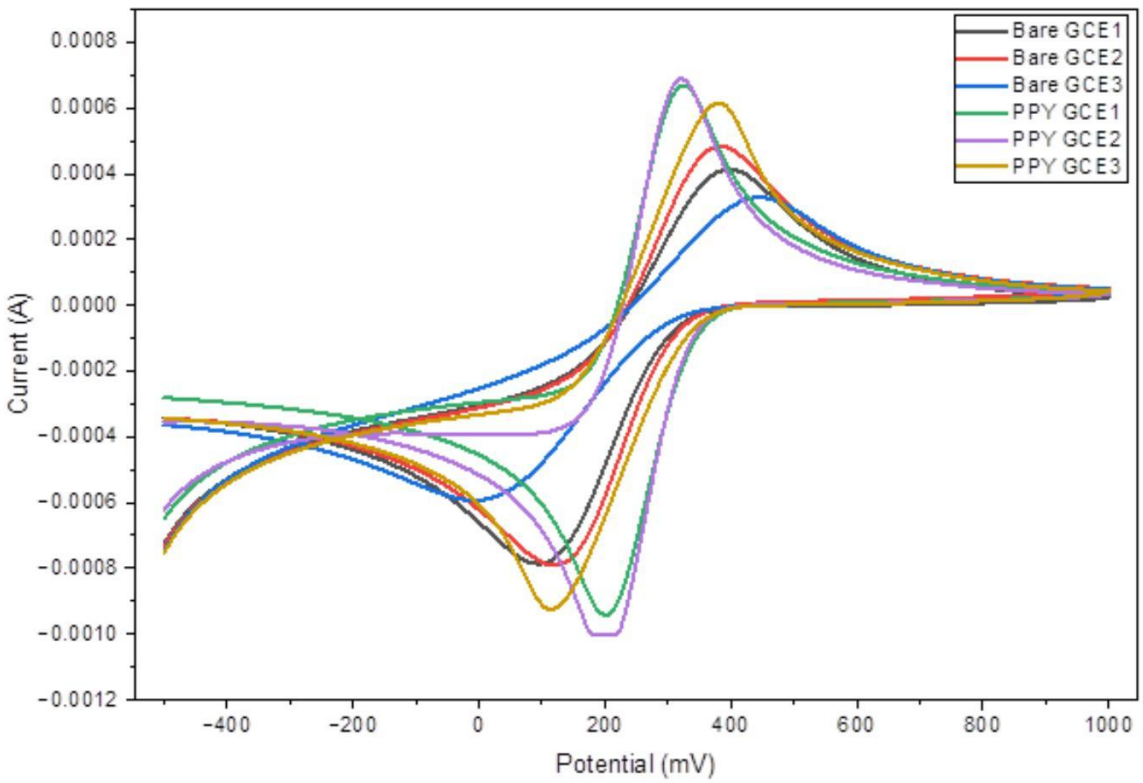

Figure 31: Cyclic Voltammetry Curves of the Bare (KFeCN) and Polypyrrole Obtained Using Three Different Glassy Carbon Electrodes

5. Conclusion

Fe_2O_3, NiO nanoparticles, and their pyrrole-based composites were effectively synthesized using green synthesis method, and their ammonia decomposition potential was evaluated. Through the presence of characteristic functional groups, FTIR data confirmed successful synthesis of the nanoparticles and successful incorporation of pyrrole. XRD structural analysis confirmed that a well-defined crystalline phase had formed, with results showing that the addition of pyrrole did not significantly affect the crystal structure of the pure nanoparticles (Fe_2O_3 and NiO), indicating effective synthesis without undesirable impurities. The synthesis of nanoparticles was further confirmed by particle size analysis, and SEM morphological analysis showed that the nanocomposite materials are more porous and have larger surface area than the pure nanoparticles, which is advantageous for increased catalytic activity. Additionally, the materials catalytic efficiency was further supported by the electrochemical results from CV, which showed good charge transfer behaviour.

Overall, the combined physicochemical and electrochemical properties confirm that the synthesized nanoparticles and their pyrrole-based nanocomposites are promising option for ammonia decomposition, with the green synthesis approach offering an added advantage for sustainable hydrogen production.

References

1. Aljuboori, A. A., Almukhtar, R. S., & Alwasiti, A. A. (2024). The bioremoval of toxic dyes using Chlorella algae in airlift bioreactor. Global NEST Journal, 26(8).
2. Atul, A. K., Srivastava, S. K., Gupta, A. K., & Srivastava, N. (2022). Synthesis and characterization of NiO nanoparticles by chemical co-precipitation method: an easy and cost-effective approach. Brazilian Journal of Physics, 52(1), 2.
3. Akhtar, K., Khan, S. A., Khan, S. B., & Asiri, A. M. (2018). Scanning electron microscopy: Principle and applications in nanomaterials characterization. In Handbook of materials characterization (pp. 113-145). Cham: Springer International Publishing.
4. Akinbami, O. M., Oke, S. R., & Bodunrin, M. O. (2021). The state of renewable energy development in South Africa: An overview. Alexandria Engineering Journal, 60(6), 5077-5093.
5. Bell, T. E., & Torrente-Murciano, L. (2016a). H2 production via ammonia decomposition using non-noble metal catalysts: a review. Topics in Catalysis, 59(15), 1438-1457.
6. Bell, T. E., & Torrente-Murciano, L. (2016b). H2 production via ammonia decomposition using non-noble metal catalysts: a review. Topics in Catalysis, 59(15), 1438-1457.
7. Berna,F.(2017).Fouriertransforminfraredspectroscopy (FTIR). Encyclopedia of Geoarchaeology, 285-286.
8. Birniwa, A. H., Abubakar, A. S., Huq, A. O., & Mahmud, H. N. M. E. (2021). Polypyrrole-polyethyleneimine (PPy-PEI) nanocomposite: An effective adsorbent for nickel ion adsorption from aqueous solution. Journal of Macromolecular Science, Part A, 58(3), 206-217.
9. Bora, N., Singh, A. K., Pal, P., Sahoo, U. K., Seth, D., Rathore, D., ... & Sarangi, P. K. (2024). Green ammonia production: Process technologies and challenges. Fuel, 369, 131808.
10. Bunaciu, A. A., UdriŞTioiu, E. G., & Aboul-Enein, H. Y. (2015). X-ray diffraction: instrumentation and applications. Critical reviews in analytical chemistry, 45(4), 289-299.
11. Chakraborty, S., Dash, S. K., Elavarasan, R. M., Kaur, A., Elangovan, D., Meraj, S. T., ... & Said, Z. (2022). Hydrogen energy as future of sustainable mobility. Frontiers in Energy Research, 10, 893475.
12. Danish, M., Ahmad, J., Muhammad, P., Javed, S., Saeed, A., Khaliq, N., ... & Ali, G. (2025). Anodic NiO nanoparticles as high-performance asymmetric supercapacitor devices in hybrid electrolytes. RSC advances, 15(53), 45665-45677.
13. Djurišić, A. B., He, Y., & Ng, A. (2020). Visible-light photocatalysts: Prospects and challenges. Apl Materials, 8(3).
14. El-Kemary, M., Nagy, N., & El-Mehasseb, I. (2013). Nickel oxide nanoparticles: Synthesis and spectral studies of interactions with glucose. Materials Science in Semiconductor Processing, 16(6), 1747-1752.
15. Elgrishi, N., Rountree, K. J., McCarthy, B. D., Rountree, E. S., Eisenhart, T. T., & Dempsey, J. L. (2018). A practical beginner's guide to cyclic voltammetry. Journal of chemical education, 95(2), 197-206.
16. Ezhilarasi, A. A., Vijaya, J. J., Kaviyarasu, K., Maaza, M., Ayeshamariam, A., & Kennedy, L. J. (2016). Green synthesis of NiO nanoparticles using Moringa oleifera extract and their biomedical applications: Cytotoxicity effect of nanoparticles against HT-29 cancer cells. Journal of Photochemistry and Photobiology B: Biology, 164, 352-360.
17. Farahmandjou, M., & Soflaee, F. (2015). Synthesis and characterization of α-Fe2O3 nanoparticles by simple co-precipitation method. Physical Chemistry Research, 3(3), 191-196.
18. Han, T., Wei, L., Xie, S., Liu, Y., Dai, H., & Deng, J. (2025). Catalyst design for ammonia decomposition: an overview. Industrial Chemistry & Materials, 3(3), 311-331.
19. Hano, C., & Abbasi, B. H. (2021). Plant-based green synthesis of nanoparticles: Production, characterization and applications. Biomolecules, 12(1), 31.
20. Hassan, Q., Algburi, S., Sameen, A. Z., Jaszczur, M., & Salman, H. M. (2024). Hydrogen as an energy carrier: properties, storage methods, challenges, and future implications. Environment Systems and Decisions, 44(2), 327-350.
21. Huang, X., Lei, K., Mi, Y., Fang, W., & Li, X. (2023). Recent progress on hydrogen production from ammonia decomposition: technical roadmap and catalytic mechanism. Molecules, 28(13), 5245.
22. Huston, M., DeBella, M., DiBella, M., & Gupta, A. (2021). Green synthesis of nanomaterials. Nanomaterials, 11(8), 2130.

23. Tom, J. UV-Vis Spectroscopy: Principle, Strengths and Limitations and Applications Article Last Updated: December 18, 2023 Written by.
24. Kirubakaran, D., Wahid, J. B. A., Karmegam, N., Jeevika, R., Sellapillai, L., Rajkumar, M., & SenthilKumar, K. J. (2026). A comprehensive review on the green synthesis of nanoparticles: advancements in biomedical and environmental applications. Biomedical Materials & Devices, 4(1), 388-413.
25. Lan, R., Irvine, J. T., & Tao, S. (2012). Ammonia and related chemicals as potential indirect hydrogen storage materials. International journal of hydrogen energy, 37(2), 1482-1494.
26. Li, J., & Li, S. (2025). Photocatalytic Synthesis in Green Chemistry: Methods and Applications. In MATEC Web of Conferences (Vol. 410, p. 03014). EDP Sciences.
27. Madheswaran, D. K., Vengatesan, S., Jegadheeswaran, S., Thangamuthu, M., Togun, H., Duraisamy, B., ... & Khan, M. W. (2025). Ammonia as a hydrogen carrier: A comprehensive analysis of electrolysis efficiency and its potential in sustainable energy systems. Renewable and Sustainable Energy Reviews, 221, 115915.
28. Makuła, P., Pacia, M., & Macyk, W. (2018). How to correctly determine the band gap energy of modified semiconductor photocatalysts based on UV–Vis spectra. The journal of physical chemistry letters, 9(23), 6814-6817.
29. Mukherjee, S., Devaguptapu, S. V., Sviripa, A., Lund, C. R., & Wu, G. (2018a). Low-temperature ammonia decomposition catalysts for hydrogen generation. Applied Catalysis B: Environmental, 226, 162-181.
30. Mukherjee, S., Devaguptapu, S. V., Sviripa, A., Lund, C. R., & Wu, G. (2018b). Low-temperature ammonia decomposition catalysts for hydrogen generation. Applied Catalysis B: Environmental, 226, 162-181.
31. Obidah Abert, H., Umaru Aduwamai, H., & Shehu Adamu, S. (2022). Effect of Green Synthesized Iron Oxide Nanoparticles Using Spinach Extract on Triton X-100-Induced Atherosclerosis in Rats. Biochemistry Research International, 2022(1), 9311227.
32. Pavithra, S., Thejas, R., Rao, H. A., Krishna, B. S., & Nagaraju, G. (2024). Preparation of polypyrrole by chemical oxidation: applications for sensor studies. Macromolecular Research, 32(1), 23-33.
33. Pei, Q., Wang, Y., Tan, K. C., Guo, J., He, T., & Chen, P. (2025). Hydrogen production via photocatalytic ammonia decomposition. Chemical Science, 16(21), 9076-9091.
34. Reda, B., Elzamar, A. A., AlFazzani, S., & Ezzat, S. M. (2025). Green hydrogen as a source of renewable energy: a step towards sustainability, an overview. Environment, Development and Sustainability, 27(12), 29213-29233.
35. Seike, M., Uda, M., Suzuki, T., Minami, H., Higashimoto, S., Hirai, T., ... & Fujii, S. (2022). Synthesis of polypyrrole and its derivatives as a liquid marble stabilizer via a solvent-free chemical oxidative polymerization protocol. ACS omega, 7(15), 13010-13021.
36. Simiyu, D. (2024). How South Africa can move on from power cuts. Nature, 632(8024), 231-231.
37. Sravanthi, M., & Manjunatha, K. G. (2021). Synthesis and characterization of conducting polypyrrole with various dopants. Materials Today: Proceedings, 46, 5964-5968.
38. Srihasam, S., Thyagarajan, K., Korivi, M., Lebaka, V. R., & Mallem, S. P. R. (2020). Phytogenic generation of NiO nanoparticles using Stevia leaf extract and evaluation of their in-vitro antioxidant and antimicrobial properties. Biomolecules, 10(1), 89.
39. Thandapani, G., Arthi, K., Pazhanisamy, P., John, J. J., Vinothini, C., Rekha, V., ... & Sekar, V. (2023). Green synthesis of copper oxide nanoparticles using Spinacia oleracea leaf extract and evaluation of biological applications: Antioxidant, antibacterial, larvicidal and biosafety assay. Materials Today Communications, 34, 105248.
40. Qiao, H., Wei, Z., Yang, H., Zhu, L., & Yan, X. (2009). Preparation and characterization of NiO nanoparticles by anodic arc plasma method. Journal of Nanomaterials, 2009(1), 795928.
41. Wong, Y. C., Wong, Y. H., Ang, B. C., Baharuddin, A. A., & Haseeb, A. S. M. A. (2023). Effects of polymerization oxidants on the fabrication of electrospun PPy/WO3 composites. Journal of Materials Science: Materials in Electronics, 34(1), 33.
42. Xi, S., Wu, W., Yao, W., Han, R., He, S., Wang, W., ... & Yu, L. (2024). Hydrogen production from ammonia decomposition: a mini-review of metal oxide-based catalysts. Molecules, 29(16), 3817.
43. Ying, S., Guan, Z., Ofoegbu, P. C., Clubb, P., Rico, C., He, F., & Hong, J. (2022a). Green synthesis of nanoparticles: Current developments and limitations. Environmental technology & innovation, 26, 102336.

Citation: Mkhonza, T.N., Nkabit , L.L. (2026). Preparat on of Fe_2O_3-Polypyrrole and NiO- Polypyrrole Nanocomposite Materials for the Photocatalyt i Generat i n of Hydrogen. *Int J Mater Sci, 2*(2), 1-23.